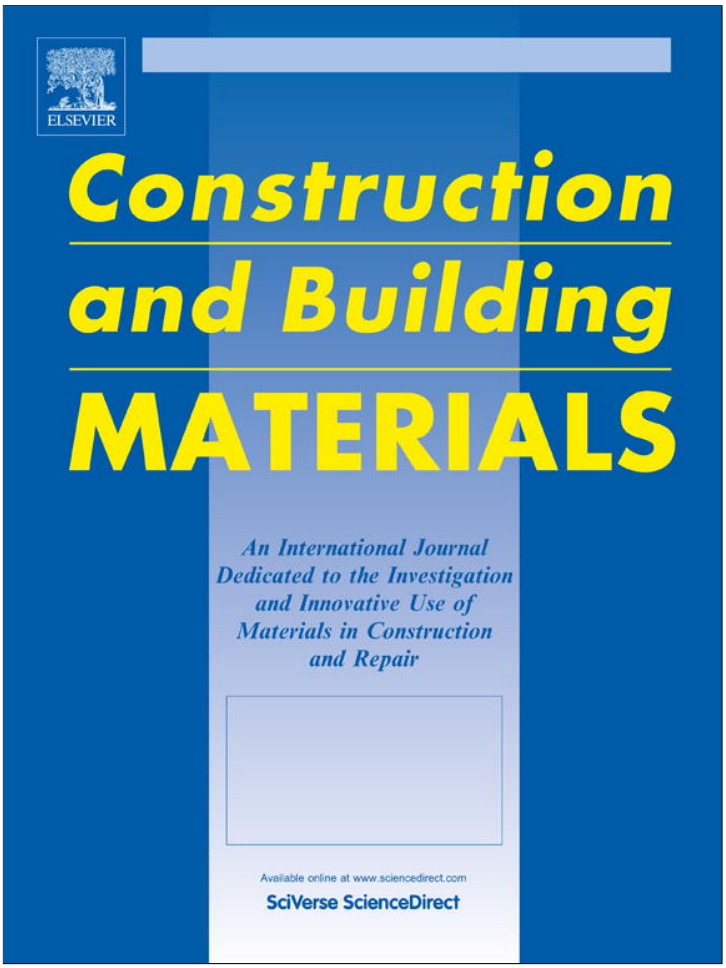

(This is a sample cover image for this issue. The actual cover is not yet available at this time.)

Construction and Building Materials 42 (2013) 248–265

Contents lists available at SciVerse ScienceDirect

Construction and Building Materials

journal homepage: www.elsevier.com/locate/conbuildmat

The influence of thermal-stressing (up to 1000 °C) on the physical, mechanical, and chemical properties of siliceous-aggregate, high-strength concrete

M.J. Heap [a,*], Y. Lavallée [b], A. Laumann [a], K.-U. Hess [a], P.G. Meredith [c], D.B. Dingwell [a], S. Huismann [d], F. Weise [d]

[a] Earth and Environment, LMU – University of Munich, Theresienstr. 41/III, 80333 München, Germany
[b] School of Environmental Sciences, University of Liverpool, Liverpool L69 3GP, United Kingdom
[c] Rock and Ice Physics Laboratory (RIPL), Department of Earth Sciences, University College London, Gower Street, London WC1E 6BT, United Kingdom
[d] BAM Federal Institute for Materials Research and Testing, Department Safety of Structures, Division Building Materials, Unter den Eichen 87, 12205 Berlin, Germany

HIGHLIGHTS

- Thermal microcracking initiates in HSC at 180 °C.
- Strength, ultrasonic velocities, Young's modulus, and Poisson's ratio decrease with increasing temperature.
- Porosity and permeability increase with increasing temperature.
- These changes are primarily the result of the thermally-induced degradation of the cement matrix.
- We provide implications for thermally-damaged HSC structures.

ARTICLE INFO

Article history:
Received 13 June 2012
Received in revised form 11 January 2013
Accepted 22 January 2013

Keywords:
High strength concrete
Fire
Thermal-stressing
Acoustic emissions
Physical properties
Elastic moduli
Uniaxial compressive strength
Indirect tensile strength
Thermo-gravimetric analysis
X-ray diffraction

ABSTRACT

High-strength concrete (HSC) will experience thermal microcracking, explosive spalling, and undesirable chemical changes when exposed to high temperatures, such as during fire, engulfment by lava flow, or nuclear meltdown. Knowledge of the resultant changes in mechanical, physical, and chemical properties is paramount for hazard mitigation. We present a multidisciplinary study on the influence of thermal-stressing on HSC. Our study shows that thermal microcracking in HSC initiates at 180 °C, is more prevalent during cooling, and exhibits the Kaiser "temperature-memory" effect. We show that residual compressive strength, indirect tensile strength, ultrasonic wave velocities, and Young's modulus and Poisson's ratio decrease, whilst porosity and permeability increase with increasing temperature. We discuss these data in terms of the chemical changes during thermal-stressing, provided by thermo-gravimetric analysis, differential scanning calorimetry, and X-ray diffraction, and from optical microscopic analysis of thermally-stressed samples. We provide implications for thermally-damaged HSC structures and a new method for non-destructive monitoring.

1. Introduction

The use of high-strength concrete (HSC) is widespread in the construction industry. Such material can be subjected to high temperatures in the event of fire, engulfment by lava flow, or nuclear meltdown. When concretes are exposed to high temperatures they are weakened by a combination of three main mechanisms. First, by chemical changes to the cement matrix, such as the dehydration/dehydroxylation of calcium silicate hydrate (C–S–H[1] gel) and calcium hydroxide (CH) at about 150 and 450 °C, respectively, and the decarbonation of calcium carbonate (at about 700 °C; decarbonation reactions will also affect any carbonate aggregates) [1–4]. Second, by thermal microcracking (see [5]). Thermal microcracks form as a result of the build-up of internal stresses due to (a) the thermal expansion mismatch between the different minerals present in the

* Corresponding author. Present address: Laboratoire de Déformation des Roches, Géophysique Expérimentale, Institut de Physique de Globe de Strasbourg (UMR 7516 CNRS, Université de Strasbourg/EOST), 5 rue René Descartes, 67084 Strasbourg cedex, France. Tel.: +33 368850039.
E-mail address: heap@unistra.fr (M.J. Heap).

[1] Cement chemist notation: C = CaO; S = SiO_2; H = H_2O.

0950-0618/$ - see front matter © 2013 Elsevier Ltd. All rights reserved.
http://dx.doi.org/10.1016/j.conbuildmat.2013.01.020

concrete aggregate, (b) thermal expansion anisotropy within individual minerals and, (c) thermal gradients (e.g., see [6]). Third, by "explosive spalling". Spalling is the product of two concomitant processes: (a) thermal dilation/shrinkage gradients and, (b) the build-up of pore pressure (see [7] and references therein).

Thermal-stressing (exposure to high temperatures) has been shown to greatly reduce the strength of concrete (reviewed by [8]). Specifically, work on HSC has shown that compressive strength [5,8–28] and tensile strength [10,18,19,25] both decrease with either increasing thermal-stressing temperature (hereafter abbreviated to TST) in residual strength testing (i.e., samples heated, cooled, and then deformed at ambient temperature) or with increasing temperature in "hot-test" strength testing (i.e., samples deformed at elevated *in situ* temperatures). Studies comparing the performance of HSC and normal-strength concretes (NSCs) have generally found that strength is reduced by a similar proportion [8–10]. The nature of the response (physical, mechanical, or chemical) of a concrete to thermal-stressing depends on its constituents and mix proportions (e.g., see [29]). Although HSC containing carbonate aggregates should intuitively suffer more at elevated temperatures [14,17,19,21–23,25,26] than those mixed with basalt, granite, or siliceous aggregates, since decarbonation will leave the aggregates intensely altered and fractured (e.g., see [30–32]), the strength of HSC containing basalt aggregates (e.g., [18]), granite aggregates (e.g., [9–12,15,16,27]), and siliceous aggregates [5,22] are still significantly reduced on exposure to high temperatures. The addition of polypropylene (PP) fibres in HSC has been shown to reduce the spalling of concrete at high temperatures (see [7] and references therein). The PP fibres melt at about 200 °C leaving the concrete more permeable and therefore less susceptible pore pressure build-up [7].

However, only one of the aforementioned studies, Huismann et al. [5], used the output of acoustic emissions (AEs) to further our understanding of the behaviour of HSC during, or after, exposure to elevated temperatures. AEs are transient elastic waves generated by the rapid release of energy within a material, such as the strain energy released during crack propagation. Hence, AE monitoring is an important diagnostic tool in material science; especially as a proxy measure for microcrack nucleation and growth during material deformation. For example, the use of AE analysis has been extensively used in other aspects of concrete research [33]. AE analysis has been used to investigate location, size orientation, and fracture mode of cracks during four-point loading of notched concrete beams [34], shear failure in large reinforced concrete beams [35], the location of tensile cracking in concrete blocks [36], the propagation of the process zone in notched concrete blocks [37], moment tensor analysis to quantitatively evaluate the fracture process in notched beams, L-shaped models and columns [38,39], salt corrosion in reinforced concrete [40], 3D location analysis [41], cyclic stressing damage both in the laboratory and by using a truck, containing different loads, to drive over beams of reinforced concrete ([42] and references therein, [43]), amongst many more. However, the use of AE output to monitor the onset temperature and extent of thermal microcracking in HSC, during both residual and "hot-test" strength testing remains, for the most part, unreported. One study, Huismann et al. [5], showed that, (1) during the heating stage of their "hot-test" experiments, the output of AE in HSC commenced at about 120 °C and continued up to 750 °C (the maximum temperature used in their study), and (2) during the loading stage, the output of AE increased as the sample approached failure. The output of AE during thermal microcracking experiments (i.e., experiments where samples are heated at a constant rate and the output of AE measured and used as a proxy for thermal microcracking, e.g., [6,44–46]) on rock samples have been previously used to track the onset temperature, the nature and extent of thermal microcracking, and the AE signature associated with phase transitions (e.g., [45]); although similar studies are rare for concrete. Interestingly, a handful of studies have demonstrated that materials can also exhibits a Kaiser "temperature-memory" effect, whereby the previous maximum temperature must be exceeded during cyclic thermal-stressing in order to generate new thermal microcracks [6,47,48]. Knowledge of the Kaiser "temperature memory" in HSC, important for concrete structures that are persistently challenged by elevated temperatures, remains unreported.

Thermal-stressing has been shown to greatly alter a wide range of material physical properties, such as permeability, Young's modulus, porosity, Poisson's ratio, and ultrasonic wave velocities (e.g., [49,50]). For HSC, research has shown that an increase in temperature leads to an increase in permeability [7,15,51–54], and a decrease in Young's modulus [5,14,17]. However, in many of these studies, the maximum temperature does not exceed 600 °C [7,14,17,52,53], permeabilities are measured indirectly using chloride-ion penetration [15,51], or empirical formula, based on the volume of micropores, are used to estimate permeability [54]. An increase of about a factor of four has been observed in the porosity of high-performance concrete (HPC) at 800 °C [11]; however, Chan et al. [11] only reported the porosity at 25 and 800 °C (and therefore do not show a complete evolution of porosity with increasing temperature). The knowledge of how physical properties change with increasing temperature in HSC is important for hazard mitigation in construction. Since, relationships derived from experimental data, such as the compressive strength of HSC for a given ultrasonic wave velocity for example, allow us to set up a system by which we can non-destructively monitor the impact of thermal damage on concrete structures.

Here therefore we present a study on the influence of high temperature (up to 1000 °C) on the physical and mechanical properties of HSC. In order to fully comprehend any observed change, we also provide analysis of the change in the chemical properties of HSC with increasing temperature. First, we describe the material and the experimental methods. We then show the output of AE (i.e., the generation of thermal microcracks) during a complete heating and cooling cycle (up to 1000 °C), including one experiment investigating the Kaiser "temperature-memory" effect in HSC. To compliment the study of Huismann et al. [5], we then present the residual strength (both compressive and indirect tensile strength) of thermally-stressed samples of the same HSC (up to 1000 °C), whilst monitoring microcracking using our fast-acquisition AE monitoring system. We then report the influence of thermal-stressing on the porosity, permeability, static and dynamic elastic moduli, and ultrasonic wave velocities of HSC. To investigate changes in HSC chemistry during heating, and to help explain any observed change in the physical and mechanical properties, we also provide thermo-gravimetric (TG) analysis, differential scanning calorimetry (DSC), and X-ray diffraction analyses (XRD). These data are also flanked by microstructural observations on thermally-stressed samples. We discuss our results in terms of hazard mitigation for concrete buildings and structures and provide a new method for the non-destructive monitoring of thermal damage.

2. Experimental material and methods

2.1. Experimental material

Our HSC was prepared using Portland cement (PC) (CEM I 42.5 R, according to EN 197-1 standards), siliceous aggregates (with a maximum diameter of 8 mm), silica fume, superplasticizer (Grace Adva Flow 391, 70% water content), PP fibres (to prevent explosive spalling of the concrete, see [7]), and a water/cement ratio of 0.32 (the same ingredients and mix proportions used by [5]). The mix proportions are given in Table 1. The connected porosity of our HSC (dried for 24 h at 100 °C) is 6.8 ± 0.15% (measured using an AccuPyc II 1340 helium pycnometer). Samples were

Table 1
Mix proportions for the high-strength concrete used in this study.

Material	(kg/m^3)
Cement CEM I 42.5 R	580
Water	173
Aggregates (siliceous)	
0–2 mm	769
2–4 mm	231
4–8 mm	538
Silica fume	63.8
Superplasticizer (Grace Adva Flow 391 (70% water content))	17.4
Polypropylene (PP) fibres	2
Total	2372.2

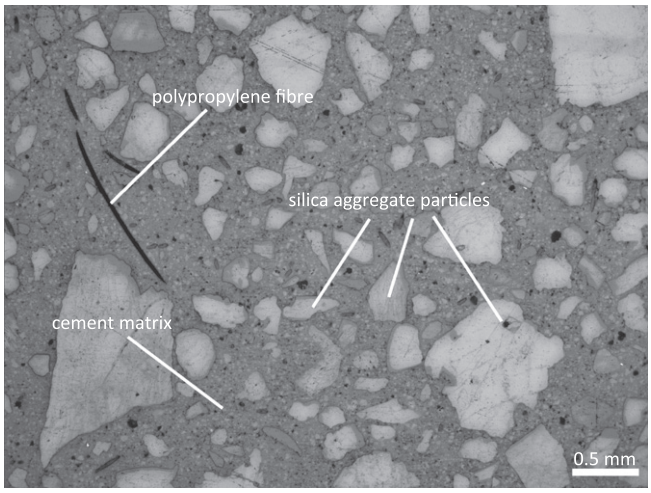

Fig. 1. Photomicrograph of the initial HSC, taken under reflected light.

all cored in the same orientation from a single set of concrete blocks, all aged for at least 285 days. A photomicrograph showing the initial HSC microstructure is shown in Fig. 1.

2.2. Monitoring the onset and extent of thermal microcracking using AE analysis

Our thermal microcracking experiments were performed in a servo-controlled, high-temperature uniaxial press at the Section for Mineralogy, Petrology and Geochemistry (LMU, Munich) (see Fig. 2 and [55] for details). The apparatus was coupled to a fast-acquisition PCI–2 based MISTRAS AE recording system, sampling at a rate of 10 MHz. AEs were recorded by two broadband PZT piezoelectric transducer crystals with a high response band over the range from 100 kHz to 1 MHz, which were mounted on the top and bottom pistons, used as waveguides (Fig. 2). Samples were cored to a diameter of 25 mm and cut parallel to a nominal length of 60 mm. A constant axial stress of about 2.2 MPa was exerted on the samples during heating to ensure a good contact between the HSC sample and the pistons. The sample temperature was monitored using a K-type thermocouple inserted into a 2 mm deep hole in the centre of the sample (Fig. 2). During experimentation, an AE hit was recorded if a signal exceeded the set threshold of 50 dB. The amplitude and absolute energy (the sum of the area under the received AE waveform envelope) of each AE signal were provided by the AEwin software.

In the first experiment, a sample of HSC was heated at a constant rate of 1 °C/min up to 1000 °C and cooled back to room temperature at the same rate. Our methodology is outlined in Fig. 3 and shows that the temperature at the centre of the sample (1) lagged slightly behind that of the furnace, and (2) reached a slightly lower peak temperature (the sample temperature peaked at 914 °C). However, Fig. 3 shows that the heating rate imposed by the furnace was accurately matched by the sample heating rate. The next experiment, to investigate the Kaiser "temperature-memory" effect, a sample of HSC was subjected to three thermal cycles under constant heating and cooling rates of 1 °C/min. The sample was first heated to a furnace temperature of 500 °C and then cooled to room temperature. It was then heated up to 700 °C and cooled again to room temperature before being subjected to a third cycle to 600 °C.

After each experiment, we calculated the cumulative output of AE energy as a function of temperature, and the evolution of the analogue seismic *b*-value. The seismic *b*-value is the negative slope of the log-linear AE amplitude-frequency distribution [56,57] here calculated using Aki's maximum likelihood method [58]

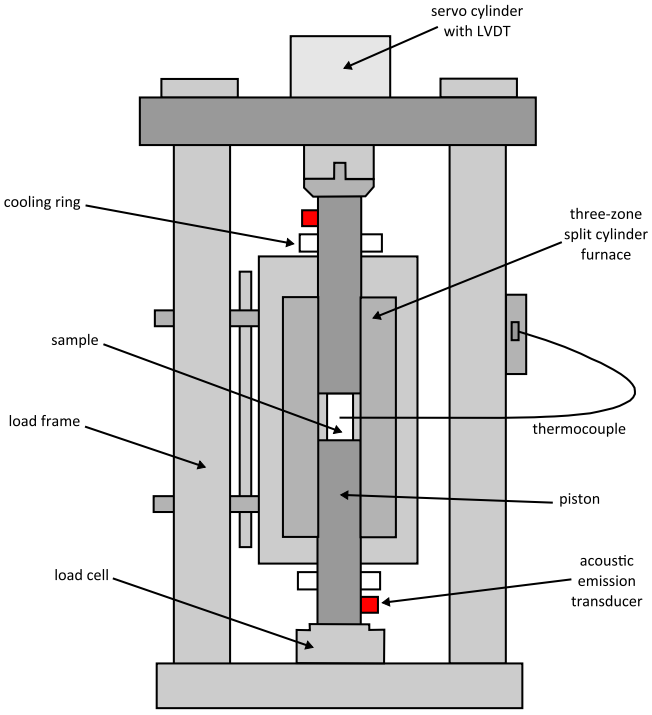

Fig. 2. Schematic diagram of the experimental arrangement used for our thermal-stressing experiments.

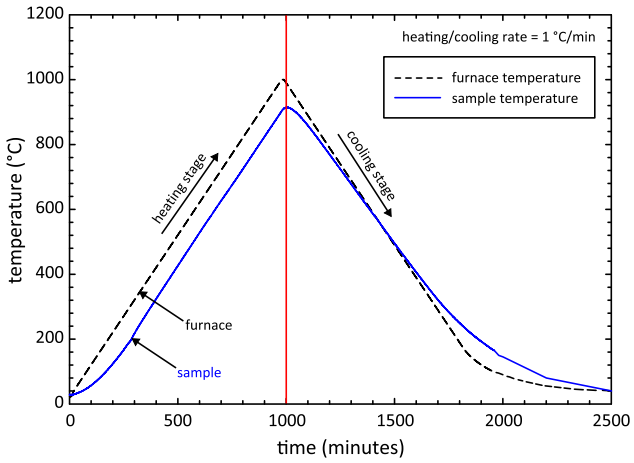

Fig. 3. A time–temperature plot outlining the methodology for our thermal-stressing experiments.

for every 200 AE hits at 100 hit intervals. Since the *b*-value describes the amplitude–frequency distribution of AE hits during a deformation process, it has also been interpreted as describing the size-frequency distribution of microcracking events in material deformation [59,60]. In particular, a decrease in the *b*-value as the level of stress is increased has been interpreted as a change from distributed, small-scale microcracking at low stress to more localised, larger-scale macrocracking in the approach to failure at high stress [60–62].

2.3. Methods to track the change in physical and mechanical properties with increasing thermal-stressing

Strength tests were performed on thermally-stressed samples using special testing jigs mounted in a servo-controlled uniaxial load-frame in the Rock and Ice Physics Laboratory (RIPL) at University College London (UCL) (Fig. 4). Experimental samples comprised cores 25 mm in diameter by 75 mm long (resulting in a length-diameter ratio of 3:1) for uniaxial compressive strength tests (UCS), and discs 40 mm in diameter by 20 mm thick for indirect tensile strength (ITS) tests (within the thickness-diameter ratio suggested by the International Society for Rock Mechanics [63]). Prior to strength testing, samples were either main-

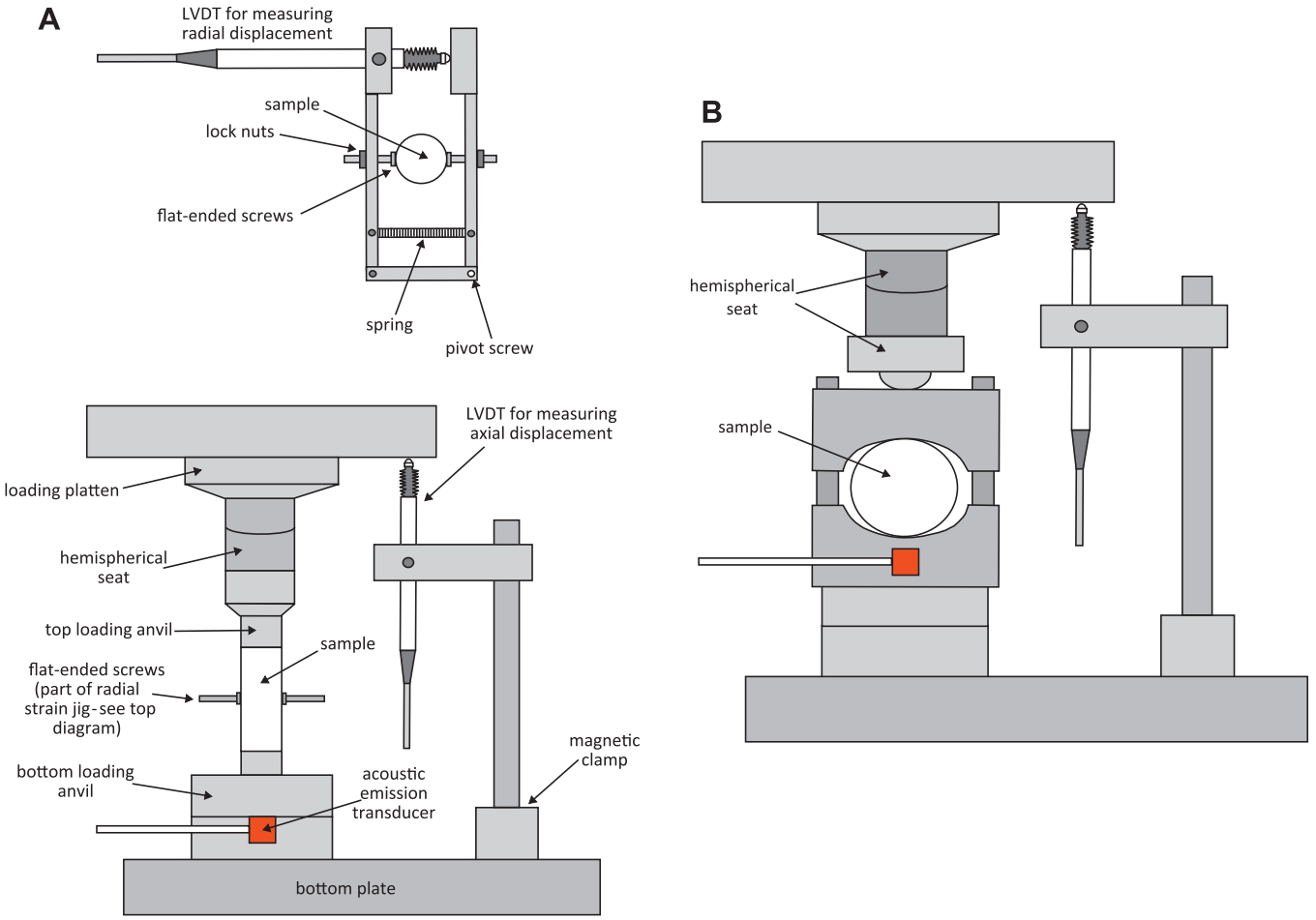

Fig. 4. Schematic diagrams of the experimental arrangement for (A) the compressive uniaxial tests, modified from [79] (top diagram: elevation showing the loading components and the positions of the axial displacement and AE transducers; bottom diagram: plan view showing the arrangement for measurement of radial displacement) and, (B) the indirect tensile strength tests.

tained at ambient temperature or thermally-stressed to a pre-determined temperature of 100, 200, 300, 500, 750, or 1000 °C. Thermal-stressing was achieved by heating the sample to the target temperature at a constant rate of 1 °C/min without load (i.e., there was no "preload"), holding the temperature constant for 60 min, and then cooling at the same rate. Thermal-stressing was conducted in an "open" system where any gaseous reaction products were free to escape. Thermally-stressed samples were left under ambient laboratory conditions for one month prior to testing. In our UCS tests, core samples were loaded at a constant strain rate of 1.0×10^{-5} s^{-1} until failure, with axial and radial strains continuously monitored using LVDT (linear variable differential transformer) displacement transducers (Fig. 4A). ITS tests were conducted using the Brazil-disc technique [63], in which discs are loaded diametrically in compression (at 1.0×10^{-5} s^{-1}) to produce a maximum tensile stress at their centre (Fig. 4B). Applied load and axial displacement were measured continuously throughout each test. Indirect tensile strengths (σ_t) were then calculated from the following relation [63]:

$$\sigma_t = \frac{2P}{\pi DL} \quad (1)$$

where P is the applied force (N) at the propagation of the first macrofracture, and D and L are the diameter (mm) and thickness (mm) of the disc, respectively.

In both UCS and ITS tests, the output of AE energy was monitored throughout via a piezoelectric transducer located in the bottom anvils of the testing jigs (Fig. 4). AE was recorded using the same system and settings as described above (apart from the signal threshold, which was set at 40 dB). After each experiment, we calculated the cumulative output of AE energy as a function of displacement or strain, and the evolution of the analogue seismic b-value (for every 200 AE hits at 100 hit intervals in our UCS tests and for every 100 hits at 50 hit intervals in our ITS tests). Static elastic moduli were also calculated for each TST, following the method of Heap and Faulkner [64]. First, each stress–strain curve was fitted with a third-order polynomial. The resultant equations were then differentiated and the slopes of the stress–strain curves (i.e., the Young's modulus) determined over their entire lengths. Both the Young's modulus and the Poisson's ratio were taken from the pseudo-linear elastic regions of such curves (i.e., those regions where the moduli did not change). We note that these values only represent one of the many elastic moduli in the deforming sample, since the elastic moduli will be developing in an anisotropic manner.

We also provide the connected porosity, ultrasonic wave velocities, dynamic elastic moduli, and permeability changes for each TST. Connected porosities were measured using an AccuPyc II 1340 helium pycnometer. Benchtop (room pressure and temperature) ultrasonic wave velocities were measured on core samples (25 mm in diameter and 75 mm in length) using a Agilent Technologies 1.5 GHz "Infiniium" digital storage oscilloscope, a JSR DPR300 35 MHz ultrasonic pulser/receiver and two custom-built sample assembly jigs that contain P- and S-wave transducers (Panametrics V103 P-wave and V153 S-wave transducers with 1 MHz resonance frequency and 0.5 in. diameter piezoelectric elements), respectively. Dynamic elastic moduli were calculated from the resultant ultrasonic wave velocities using the following formula:

$$E = \rho \frac{V_s^2(3V_p^2 - 4V_s^2)}{V_p^2 - V_s^2} \quad (2)$$

$$\nu = \frac{V_p^2 - 2V_s^2}{2(V_p^2 - V_s^2)} \quad (3)$$

where ρ is the bulk sample density and V_p and V_s are the P- and S-wave velocities, respectively. In this case, and unlike the microcrack damage as a result of uniaxial stressing, thermal microcracking, and therefore changes in elastic moduli, is generally expected to be relatively isotropic [49].

Water permeability measurements were made in a 300 MPa hydrostatic pressure vessel (located in the Rock and Ice Physics Laboratory (RIPL) at University College London, UCL) equipped with two 70 MPa servo-controlled pore fluid (distilled water) intensifiers or volumometers (Fig. 5) on cylindrical samples 25 mm in diameter by 30 mm long (for further information on the testing equipment see [65]). All

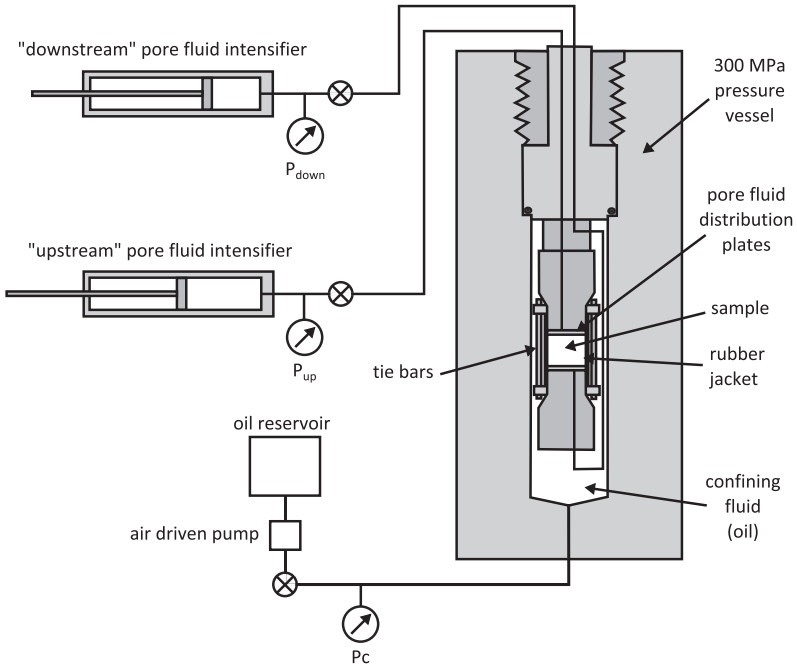

Fig. 5. Schematic diagram of the experimental arrangement for our permeability measurements. "P_c" = confining pressure; "P_{up}" = upstream pore fluid pressure; "P_{down}" = downstream pore fluid pressure".

samples were vacuum saturated in distilled water prior to experimentation. Once inside the setup, the confining pressure (P_c) and the pore fluid pressure (P_p) were increased to 10 and 5 MPa, respectively. The samples were left for 30 min at an effective pressure (for the purpose of this study we apply the simple effective pressure (P_{eff}) law of $P_{eff} = P_c - \alpha P_p$, assuming that $\alpha = 1$ [66]) of 5 MPa to ensure microstructural equilibration and complete saturation. The two volumometers were then used in an "upstream" (P_{up}) and "downstream" (P_{down}) configuration, with a 1 MPa pressure difference across the sample to provide the flow required to calculate water permeability (κ_{water}) using Darcy's law:

$$\frac{Q}{A} = \frac{\kappa_{water}}{\eta L}(P_{up} - P_{down}) \quad (4)$$

where Q is the volume of fluid measured per unit time, A is the cross-sectional area of the sample, η is the viscosity of the pore fluid, and L is the length of the sample. P_{up} and P_{down} were set at 4.5 and 5.5 MPa, respectively. The volumometers were allowed to move full stroke (10 cm^3) and steady-state flow was only assumed when the flow rate was constant over a protracted period.

2.4. Methods to track the change in chemical properties with increasing thermal-stressing

Thermo-gravimetric (TG) analysis and differential scanning calorimetry (DSC) were used to track the chemical changes in HSC during thermal-stressing. TG analysis tracks the mass loss during heating, while DSC monitors the amount of heat required to increase the temperature of the sample (and therefore indicates when the sample undergoes a physical transformation, such as a phase transition). Both analyses were carried out simultaneously using the Netzsch STA 449 C thermobalance apparatus at the Section for Mineralogy, Petrology and Geochemistry (LMU, Munich). Powdered samples (of approximately 40 mg, taken from a larger batch of well-mixed powder [approximately 500 g] so as to not introduce a bias into our measurements), of the initial material and samples thermally-stressed to each TST, were heated in an air atmosphere in a platinum crucible (with lid) at a heating rate of 10 °C/min up to a temperature of 100 °C. The samples were then left at 100 °C for 60 min, to ensure they were completely free of non-chemically bound water. Samples were then heated to a target temperature of 1000 °C, again at 10 °C/min, and then cooled at the same rate.

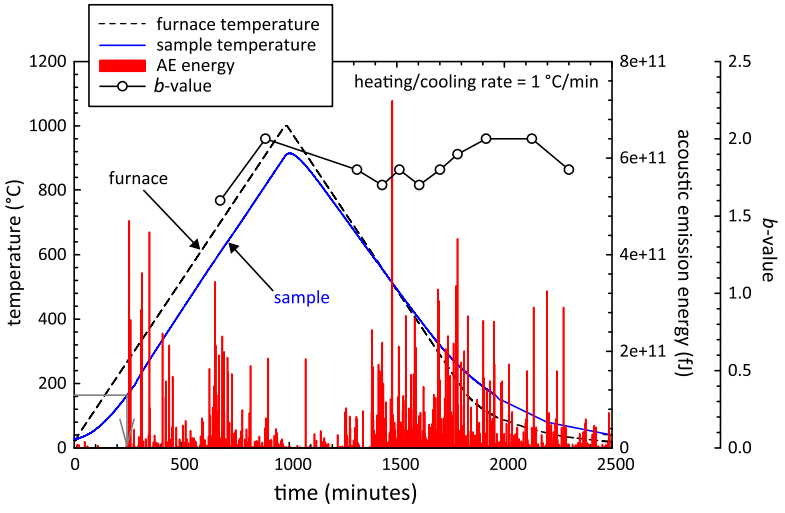

Fig. 6. The output of AE energy during a thermal-stressing experiment conducted at a thermal-stressing rate of 1 °C/min on a sample of HSC. The sample was heated to 1000 °C and then cooled back to ambient temperatures at the same rate. Seismic b-values are calculated using Aki's maximum likelihood method [58] for 200 hits at 100 hit intervals.

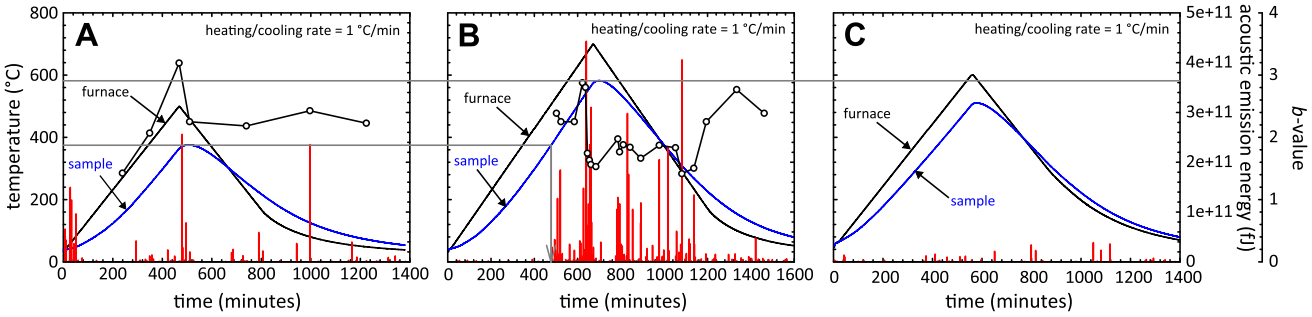

Fig. 7. The output of AE energy during a thermal-stressing experiment on a sample of HSC that contained three successive heating and cooling cycles. All three cycles were conducted using a heating/cooling rate of 1 °C/min. The sample was heated to (A) 500 °C, (B) 700 °C, and finally (C) 600 °C. Seismic *b*-values are calculated using Aki's maximum likelihood method [58] for 200 hits at 100 hit intervals.

2.5. Microstructural analyses

Samples of thermally-stressed HSC were also prepared for microstructural analysis. Samples were first heated to TSTs of 100, 200, 300, 500, 750, and 1000 °C at a rate of 1 °C/min, left at the target temperature for 60 min, and cooled to ambient temperatures at the same rate. Upon returning to ambient temperature, they were then set in epoxy resin. Once cured, thin sections were then prepared for optical microscopy analysis using a Leica DM2500 (equipped for both transmitted and reflected light) microscope with a mounted 5 megapixel Leica DFC425 digital camera. The samples were set in first set in resin to avoid any secondary mineral growth during thin section preparation. For comparison, a sample of the initial material was also prepared for microscopic analysis.

3. Results

3.1. Thermal microcracking in HSC

The output of AE, i.e. the generation of thermally-induced microcracks, during the thermal-stressing of HSC is shown in Fig. 6. Our results demonstrate that thermal microcracking was prevalent above sample temperatures of about 180 °C (denoted by the grey arrow) and continued until the sample reached ambient temperature. We also observe a greater proportion of thermal microcracking during the cooling phase of the experiment. Further, *b*-values (the negative slope of the log-linear AE frequency–magnitude) remain consistently high (in general, between 1.8 and 2.0) and are independent of sample temperature.

3.2. Observation of the Kaiser "temperature-memory" effect in HSC

The Kaiser "temperature-memory" effect was investigated in HSC during a thermal cycling experiment, with successive thermal-stressing peak temperatures of 500, 700, and 600 °C (Fig. 7). The AE data show that HSC displays the Kaiser "temperature-memory" effect. During heating in the second cycle, the output of AE recommenced only when the sample temperature exceeded the peak previously reached in the first cycle (denoted by the grey arrow). During the third cycle, where the sample temperature did not exceed that of any previous cycle, very few AEs were recorded (Fig. 7C).

3.3. Compressive and tensile strength in HSC with increasing thermal-stressing

Plots of stress, cumulative AE energy (ΣAE), and *b*-value against strain for each of our UCS tests are presented in Fig. 8 (and synopsis plots are available in Fig. 9). Similarly, plots of force, ΣAE, and *b*-value against loading ram displacement for our Brazil-disc tensile tests are presented in Fig. 10 (and synopsis plots are available in Fig. 11). The changes in residual UCS and ITS as a function of TST are then summarised in Fig. 12, and images of deformed samples, showing characteristic failure modes for low TST tests (300 °C and below) and high TST tests (above 300 °C), are presented in Fig. 13.

The data of Figs. 8–11 demonstrate that both strength and mode of failure change as the TST is increased. At lower TSTs (300 °C and below), failure is rapid and catastrophic and the failure mode is axial splitting (Fig. 11). We observe very little deviation from pseudo-linear elastic deformation prior to peak stress/force and failure in the mechanical data, and very little AE output until just prior to failure, where the rate accelerates dramatically (Figs. 8–11). This behaviour can be described as macroscopically brittle (i.e., the ability of the rock to resist load decreases with permanent strain, see [67]). Furthermore, we note that the axial (compressive) and diametral (tensile) macrocracks formed at failure propagate through both the PC matrix and the siliceous aggregates with little deviation (Fig. 13), a feature diagnostic of very rapid fracture propagation (see also [68]). By contrast, the deformation of samples heated to higher TSTs (above 300 °C) becomes progressively less macroscopically brittle (although, by definition, the samples are still brittle, see [67]). For the compressive tests, we observe considerable deviation from linearity prior to peak stress in the mechanical data, and a significant degree of stain softening after peak stress before failure occurs (Fig. 9A). We note that the onset of significant AE output generally commences at the same time as the deviation from pseudo-linear behaviour, and increases at a more gradual rate (Fig. 9C). This general pattern is summarised in the synoptic stress–strain plots (Fig. 9A and B), which show that not only does the failure stress decrease dramatically with increasing TST above 300 °C, but that the strain at failure increases markedly. Results for the tensile tests at higher TST show essentially similar behaviour (Figs. 10 and 11), with distinct breaks of slope in the force–displacement curves that correspond to the onset of significant AE output. These inflections correspond to the points of first fracture (i.e., the point where the first tensile macrofracture traverses the sample, and are marked on the figure with red arrows). The resulting macrocracks in the high TST (above 300 °C) samples (Fig. 13) are seen to be more convoluted; they propagate only through the PC matrix, passing around the siliceous aggregates. These observed differences in failure mechanism between low and high TST samples are also reflected in the contrasting behaviour of the seismic *b*-values. For low TST tests (below 300 °C), *b*-values decrease rapidly from relatively high values around 1.5 to low values around 0.5 for both compressive and tensile failure. This is symptomatic of a change from distributed microcracking to localised macrocracking as failure is approached [59,60,69]. By contrast, for high TST tests (above 300 °C), *b*-values remain essentially constant with high values in the range 1.5–2.0, indicative of distributed microcracking throughout. The *b*-values for the tests at the intermediate TST of 300 °C appear to exhibit transitional behaviour, with a decrease from around 1.5 to 1.0 as failure is approached. Volumetric strains, computed from the axial and ra-

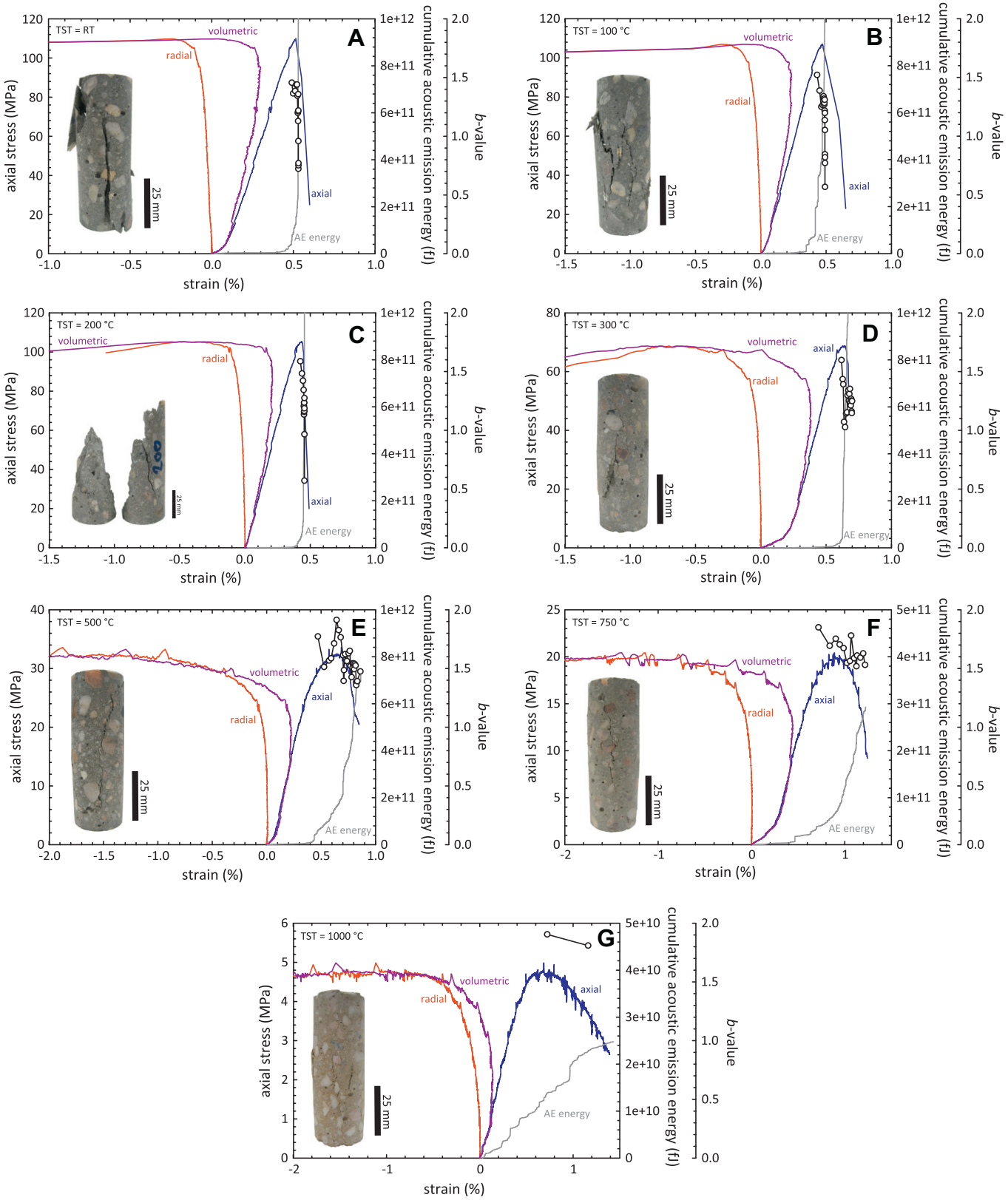

Fig. 8. Stress–strain curves (axial, radial and volumetric) for each of the constant strain rate (1.0×10^{-5} s^{-1}) compressive residual strength tests on a sample of the initial HSC (A) RT, and samples thermal-stressed to temperatures of (B) 100 °C, (C) 200 °C, (D) 300 °C, (E) 500 °C, (F) 750 °C and, (G) 1000 °C. Cumulative AE energy output and *b*-values (calculated using Aki's maximum likelihood method [58] for 200 hits at 100 hit intervals) are also plotted for each test. Photographs of the post-failure samples, showing their macroscopic failure mode, are also provided on each of the graphs. Note that the scales on some of the axes differ; this is to better demonstrate the form of the curves. Direct comparisons can be made in the synopsis plots of Fig. 9.

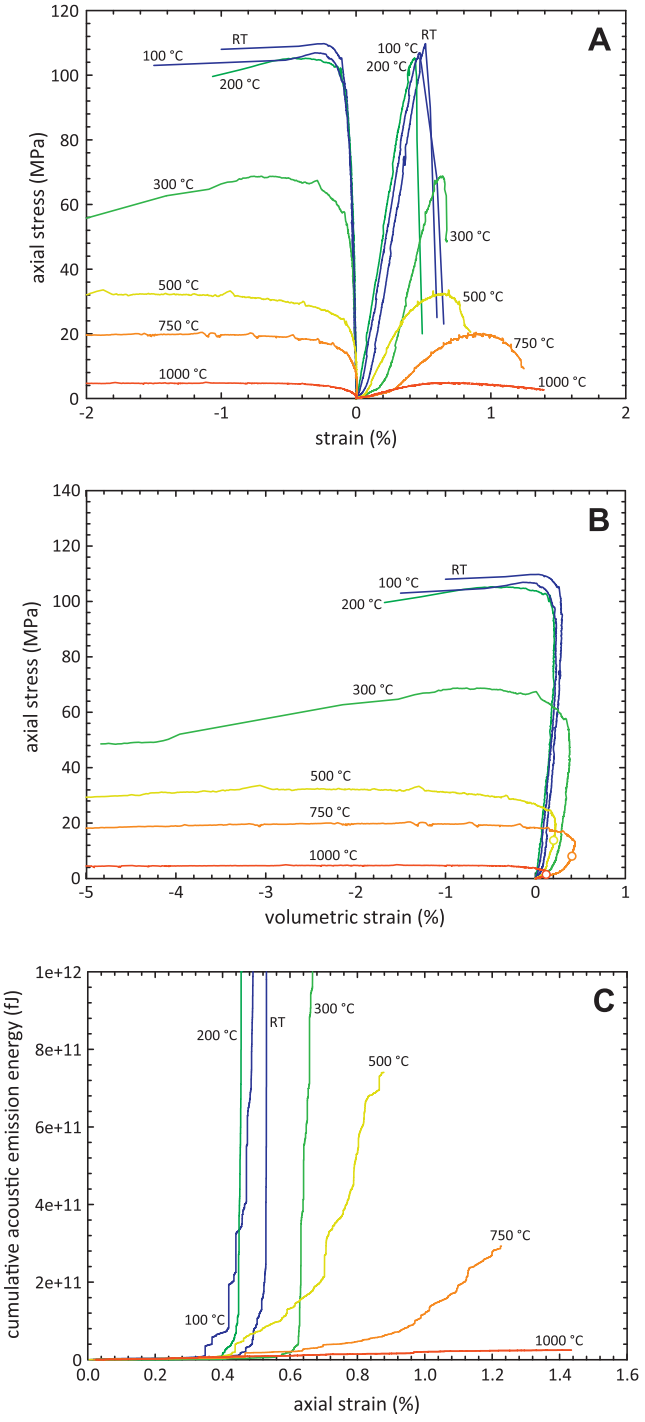

Fig. 9. Synoptic plots of the data from the UCS tests. (A) A synoptic plot of all of the axial strain curves; (B) a synoptic plot of all of the volumetric strain curves (including the position of C′ for 500, 750, and 1000 °C); (C) a synoptic plot of all of the cumulative AE curves.

dial strains, are also provided for our UCS tests (Fig. 9B). They also demonstrate that, as the TST increases, the deformation style is progressively less macroscopically brittle. Also included in Fig. 9B are the positions of C', the onset of dilatancy (i.e., the onset of a relative increase in sample volume, see [70]), for TSTs of 500, 750, and 1000 °C. The stress at which C' occurs decreases with increasing TST.

Residual UCS and ITS with increasing TST are summarised in Fig. 12A and B, respectively, together with UCS data from the "hot-tests" of Huismann et al. [5] on the same material. We observed only small (<10%) reductions in both residual UCS and ITS for TSTs up to 200 °C, but significant decreases for TSTs of 300 °C and above. Over the entire range of TSTs, the UCS was reduced by about 96% (from about 109 MPa to about 4.5 MPa) and the ITS by about 90% (from about 11.5 MPa to about 1 MPa). The ratio of uniaxial compressive to tensile strength in our experiments is close to that predicted by the extended Griffith criterion, i.e. close to 12 [71]. We also note that the residual values of UCS are consistently lower than the "hot-test" strengths of Huismann et al. [5].

3.4. Porosity, permeability, ultrasonic wave velocities, and dynamic and static elastic moduli in HSC with increasing thermal-stressing

The connected porosity of HSC increases substantially with increasing TST (Fig. 14A). Over the entire temperature range, from RT (room temperature) to 1000 °C, the connected porosity increased from 6.8% to 22.7% (an increase by about a factor of three). Water permeability was seen to increase by five orders of magnitude (Fig. 14B), from 7.2×10^{-20} m^2 to 1.9×10^{-14} m^2, and ultrasonic wave velocities both decreased by roughly a factor of two, from 4.7 to 2.8 km s^{-1} and from 3.2 to 1.8 km s^{-1} for P- and S-wave velocity, respectively (Fig. 14C). Dynamic Young's modulus decreased from 50.2 to 15.6 GPa (a total decrease of 60%) and static Young's modulus decreased from 27.6 to 0.8 GPa (to total decrease of 85%) (Fig. 14D). Dynamic Poisson's ratio decreased from 0.15 to 0.04 (a total decrease of 74%) and static Poisson's ratio decreased from 0.11 to 0.04 (to total decrease of 68%) (Fig. 14D). As a general trend, changes in the physical properties of HSC with increasing TST are modest until 200 °C, after which the rate of change increases significantly.

3.5. Chemical changes in HSC with increasing thermal-stressing

To identify any chemical changes and phase transitions during thermal-stressing, TG (Fig. 15A), and DSC (Fig. 15B) analyses were performed on a powdered sample of HSC kept at ambient temperature (RT) and powdered samples thermally-stressed to TSTs up to 1000 °C. Our DSC analysis identified four main endothermic peaks during heating, between 140–160 °C, between 440–480 °C, at exactly 573.5, and between 650–740 °C (labelled (1), (2), (3), and (4) in Fig. 15B). The peak between 140 and 160 °C became less and less pronounced as the TST increased up to 300 °C; after 300 °C there was little change in the magnitude of the peak. The peaks between 440–480 °C and between 650–740 °C disappeared in samples thermally-stressed to 500 °C and above, and 750 °C and above, respectively (implying that both reactions are non-reversible). However, the peak at 573.5 °C is present, and of the same amplitude, regardless of the TST. There were also endothermic peaks at about 240 and 410 °C. The peak at 240 °C was pronounced in the RT sample and the sample thermally-stressed to 100 °C, became a shoulder at 200 °C and was not present at TSTs of 300 °C and above. The peak at 410 °C, albeit small, remained regardless of the TST.

Our TG analysis shows that, for the RT sample, there was total reduction of about 7% mass upon heating to 1000 °C (and this reduction was reduced as TST is increased). The mass lost prior to 100 °C, where the measurements started, was also reduced as TST increased. At 750 and 1000 °C, very little change in mass was observed over the entire heating range. The four main endothermic reactions (as evidenced by our DSC) are also labelled (1), (2), (3), and (4) on Fig. 15A. Since there is a continuous decrease (with the exception of the samples thermally-stressed to 750 and 1000 °C) in sample mass with increasing temperature, it is difficult to determine whether the four main endothermic reactions had a direct impact on mass loss. Circumstantial evidence suggests that reaction (1) resulted in a large decrease in mass (there

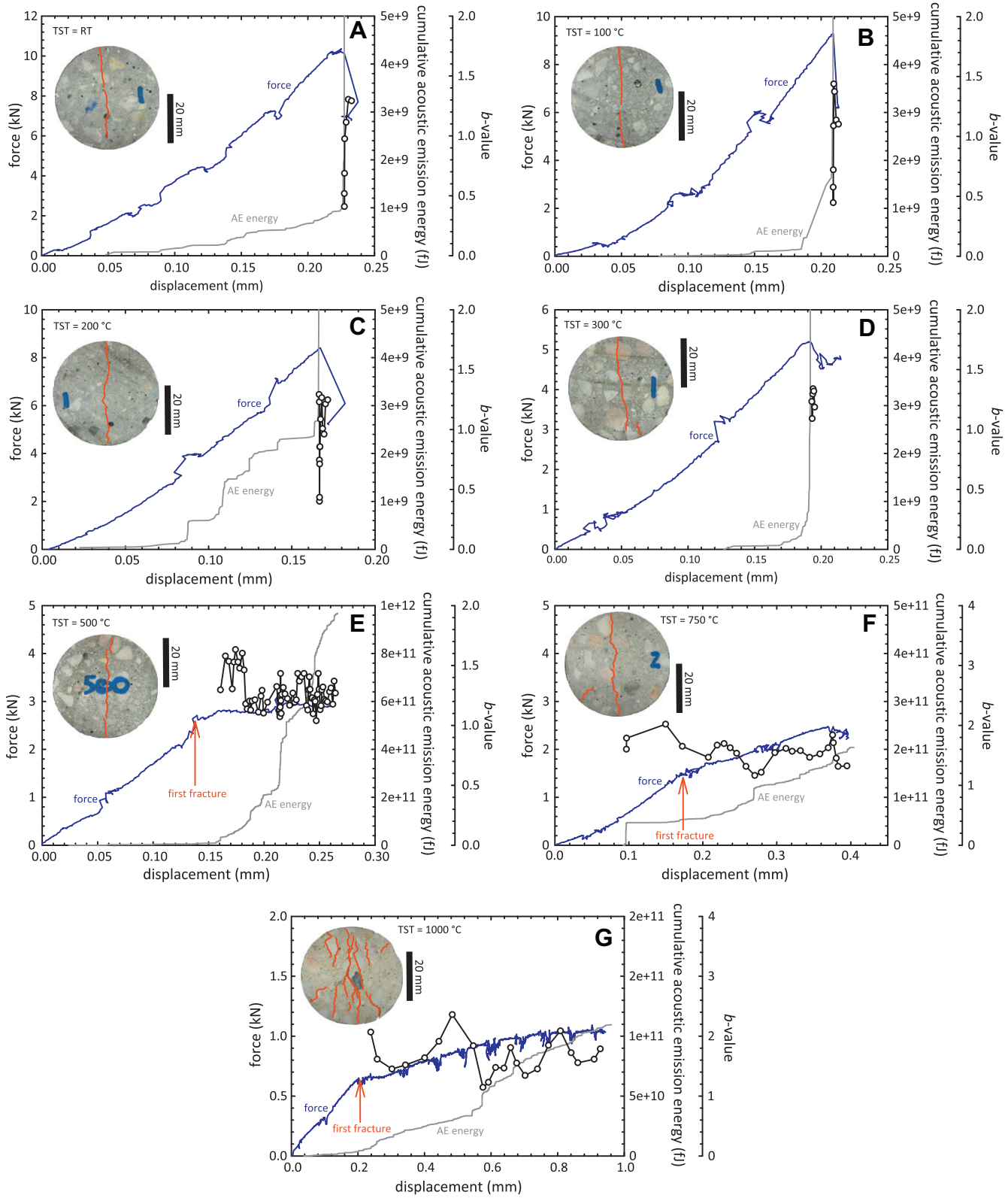

Fig. 10. Force–displacement curves for each of the tensile "Brazil disc" tests on a sample of the initial HSC (A) RT, and samples thermal-stressed to temperatures of (B) 100 °C, (C) 200 °C, (D) 300 °C, (E) 500 °C, (F) 750 °C and, (G) 1000 °C. Cumulative AE energy output and *b*-values (calculated using Aki's maximum likelihood method [58] for 100 hits at 50 hit intervals) are also plotted for each test. Photographs of the post-failure samples, showing their macroscopic failure mode are also provided on each of the graphs (macrocracks are highlighted in red). Note that the scales on some of the axes differ; this is to better demonstrate the form of the curves. Direct comparisons can be made in the synopsis plots of Fig. 11. (For interpretation of the references to color in this figure legend, the reader is referred to the web version of this article.)

is a large decrease in mass before any other reactions are indicated via DSC). Reaction (2) appears to increase the rate of mass loss for a short period; however, this influence disappears at temperatures of 500 °C and above. Immediately after reaction (3) the rate of mass loss increases before reaching reaction (4), where the rate of mass loss is reduced. The mass loss commensurate with

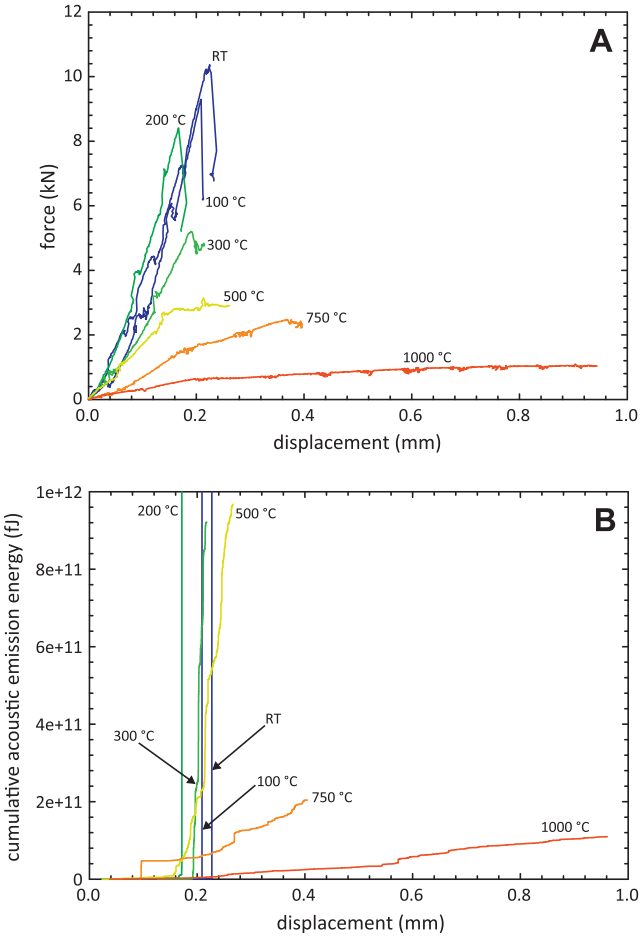

Fig. 11. Synoptic plots of the data from the ITS tests. (A) A synoptic plot of all of the force–displacement curves; (B) a synoptic plot of all of the cumulative AE curves.

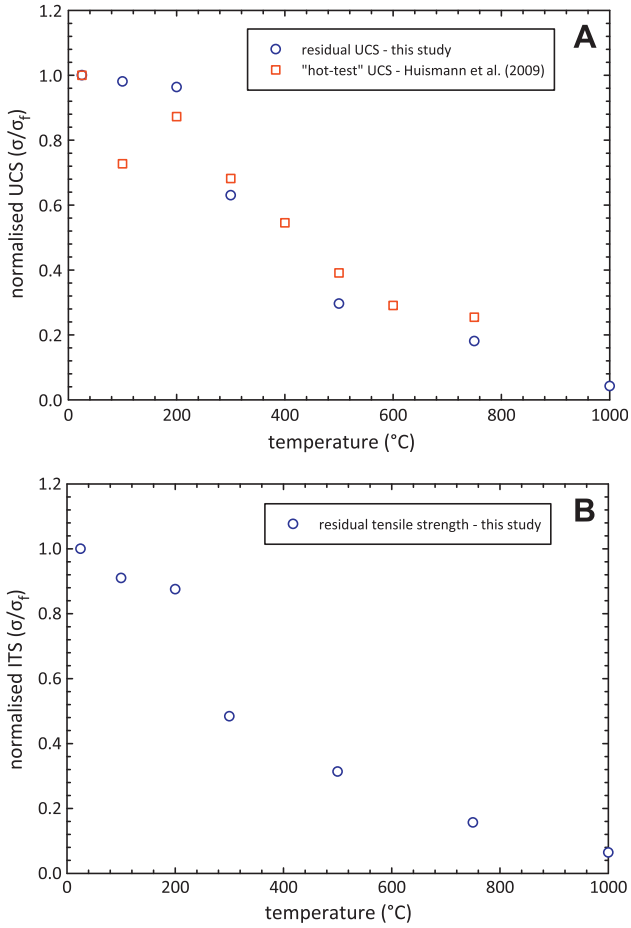

Fig. 12. The influence of thermal-stressing temperature (TST) on (A) the residual compressive strength of HSC, and (B) the residual indirect tensile strength of HSC. "Hot-test" data from Huismann et al. [5], using the same HSC, are also plotted in (A).

reactions (3) and (4) disappears at temperatures of 750 °C and above.

3.6. Microstructural analysis of thermally-stressed HSC

Microstructural observations on thermally-stressed samples (to TSTs of 100, 200, 300, 500, 750, and 1000 °C) of HSC are shown in Fig. 16. The initial material (TST = RT, Fig. 16A) has also been included for comparison. Optical microscopic analysis has demonstrated that there were no major changes in HSC microstructure until 300 °C, where small microcracks were observed, usually found in the PC matrix close to silica aggregate particles (Fig. 16E). The microstructure at 500 °C was found to contain more microcracks than seen at 300 °C. Larger microcracks within the PC matrix were seen at 750 °C (Fig. 16H) and, at 1000 °C, extensive microcracking (Fig. 16H) and an eroded "sponge-like" texture (Fig. 16J) were observed, again within the PC matrix. In general, the microcracking seen within the silica aggregate particles did not increase significantly with increasing TST.

4. Discussion

4.1. Temperature-induced chemical changes/phase transitions in HSC

For the purpose of the rest of the discussion, the results of the chemical analyses (i.e., the TG and DSC analysis) will be discussed first. The four main endothermic peaks (at 140–160, 440–480, exactly 573.5, and 650–740 °C) have been labelled on Fig. 15. The first of the four (labelled (1) in Fig. 15), between 140 and 160 °C, is likely to be due primarily to the loss of water from C–S–H gel in the PC matrix. As TST is increased, less and less bonded water exists, explaining why the peak becomes progressively smaller up to 300 °C. However, above 300 °C, the amplitude of the peak is unaffected, highlighting that the reaction is partially reversible (i.e., some of the water lost from C–S–H gel is reclaimed post-heating). The loss of bonded water results in a large decrease in the mass of the sample (Fig. 15A). At 200 °C (before the onset of any other reaction, as indicated by our DSC) the loss in sample mass of about 3% represents a large proportion of the total mass loss of 7%. We must note that, although the most likely explanation of the endothermic peak between 140 and 160 °C is the dehydration of C–S–H gel, a temperature between 140 and 160 °C is actually rather high when compared to previously published values [2,4]. For instance, Sha et al. [2], who used the same heating rate as this study, found a value closer to 110 °C. We suggest that this discrepancy may be due to (1) subtle differences in cement mixture, (2) our concrete blocks are aged to at least 285 days (those of Sha et al. [2] ranged between 15 and 45 days) and, (3) differences in experimental program (in our experiments we stalled at 100 °C for 60 min prior to heating to ensure they were completely free of non-chemically bound water).

The peak between 440 and 480 °C (labelled (2) in Fig. 15) is due to the dehydroxylation of CH, a hydration product, in the PC matrix. At this temperature, CH decomposes to calcium oxide or

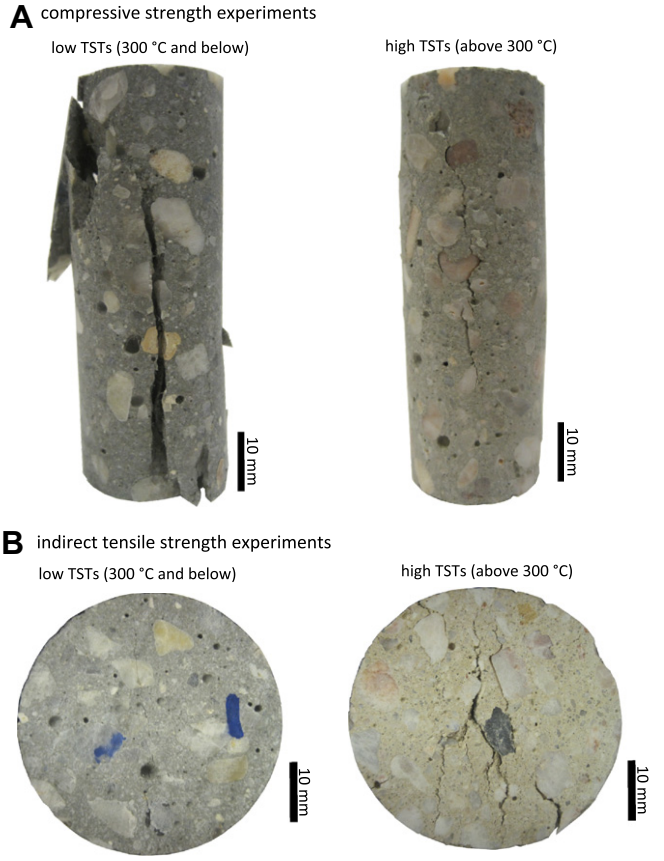

Fig. 13. Photographs of the typical failure modes at low (300 °C and below) and high (above 300 °C) thermal-stressing temperatures (TSTs) in (A) compression and (B) tension.

"lime" (C) and water. The fact that the reaction disappears at TSTs above 500 °C (Fig. 15B) indicates that the reaction is non-reversible. This reaction is associated with a short increase in the rate of mass loss (Fig. 15A).

The third main peak (labelled (3) in Fig. 15), at exactly 573.5 °C, is due to the α/β transition in the siliceous aggregates and the silica fume. This agrees with previous studies on the α/β transition in quartz [45]. The reaction does not disappear, even at the highest TST of 1000 °C. Since the α/β transition in quartz does not involve a loss of mass, it cannot explain the increase in the rate of mass loss seen at a temperature of about 570 °C (Fig. 15A). The α/β transition in quartz involves a sudden volumetric expansion that is normally commensurate with an increase in microcracking in quartz-rich rocks, as measured by the output of AE [45]. However, for our HSC samples, we do not see a large spike in the output of AE at 573.5 °C (Fig. 6). Further, microstructural analysis showed that the microcracking seen within the siliceous aggregates did not increase significantly with increasing TST (Fig. 16), an observation also observed in SEM studies of thermal damage in concretes [72].

The forth main peak (labelled (4) in Fig. 15), between 650 and 740 °C, is associated with the decarbonation of calcium carbonate of the PC matrix, together with possible solid–solid phase transformations [1]. Calcium carbonate decomposes to calcium oxide or "lime" (C) and carbon dioxide at temperatures above 700 °C [3,73]. The fact that the reaction disappears at TSTs above 750 °C (Fig. 15B) indicates that the reaction is non-reversible. Although the decarbonation of calcium carbonate has been observed previously for PC [2], it may be considered surprising, since (1) the main ingredient of PC is calcium oxide (C, the product of the decarbonation of calcium carbonate) and, (2) our HSC contains siliceous aggregates. In an attempt to resolve this discrepancy, X-ray diffraction (XRD) analysis was performed on powdered samples of HSC [on an initial sample (i.e., RT) and samples that had been thermally-stressed to each TST] (Fig. 17A). The analysis was performed in transmission geometry on a Stoe Kristalloflex diffractometer (Cu Kα1-radiation λ = 1.544056 Å, curved Ge (1 1 1) monochromator) at the Section for Mineralogy, Petrology and Geochemistry (LMU, Munich). The step size for the measurements was 0.01° 2θ, the measurement range was between 2θ angles of 27° and 32° (in order to accurately capture the peak of calcite and to avoid the signal becoming oversaturated by that of quartz), the step time was 30 s, and the scan rate 0.02°/min. The XRD spectra of Fig 17A clearly show that the peak for calcite (at a 2θ angle of about 29.5) is present for the sample at RT, and those up to a TST of 500 °C. However, the calcite peak disappears in the samples thermally-stressed to 750 and 1000 °C. These data confirm that decarbonation of calcium carbonate does occur in our siliceous-aggregate HSC and must be due to the presence of calcium carbonate within the PC matrix. To confirm that the dehydration/dehydroxylation of C–S–H gel and CH had progressed, we ran an additional XRD analysis on a powdered sample of PC (i.e., not powders made from the entire sample, as for the TG/DSC analysis, and the above XRD analysis) that had been thermally-stressed to 1000 °C (Fig. 17B). For this run, the measurement range was between 2θ angles of 5° and 60° (the step size was the same as described above, but the step time was reduced to 10 s, resulting in a scan rate of 0.06°/min). The XRD spectra of Fig. 17B show peaks for both bi- and tri-calcium silicates (C2S and C3S, products of the dehydration of C–S–H) and calcium oxide (C, a product of the dehydroxylation of CH). Further, the eroded "sponge-like" texture seen at 1000 °C (Fig. 16) has been previously attributed to the decarbonation of calcium carbonate [73–75].

The peak seen at 240 °C is likely to be due to the formation of calcium aluminate hydrate (a hexagonal hydrate) from tricalcium aluminate, which is then likely to form ettringite (another hexagonal hydrate) in a reaction between the newly formed calcium aluminate and the calcium sulphate in the PC matrix. The formation of hexagonal hydrates is affected by thermal-stressing and, even at TSTs as low as 300 °C, we do not see the peaks associated with the formation of hexagonal hydrates. The peak at about 400 °C, unaffected by TST, is likely to be due to the formation of Fe_2O_3 solid solution from tetracalcium aluminoferrite. Previous studies have shown further endothermic peaks, associated with the formation of other hexagonal hydrates at about 170 °C [1] and iron-substituted ettringite at about 150 °C [1,2]. However, in our data, we do not observe these peaks. It is likely that they are masked by the large peak associated with the loss of water from C–S–H gel.

4.2. Temperature-induced physical and mechanical properties changes in HSC

The results from both our compressional and tensile experiments demonstrate that the variation in strength of HSC samples thermally-stressed to temperatures up to 200 °C is extremely small. However, above 200 °C, both strengths deteriorate markedly. Changes in the other measured physical properties (connected porosity, permeability, ultrasonic wave velocities, and static and dynamic elastic moduli), in general, also mirror this trend. These results can be explained by (1) AE analysis has shown that 180 °C represents the lower limit for the initiation of thermal microcracking (Fig. 6), corroborated by our microstructural observations (we observe thermal microcracks within the PC matrix of our HSC samples thermally-stressed to 300 °C and above, see Fig. 17) and, (2) chemical changes to the PC matrix, such as dehydroxylation of calcium hydroxide (between 440 and 480 °C) and

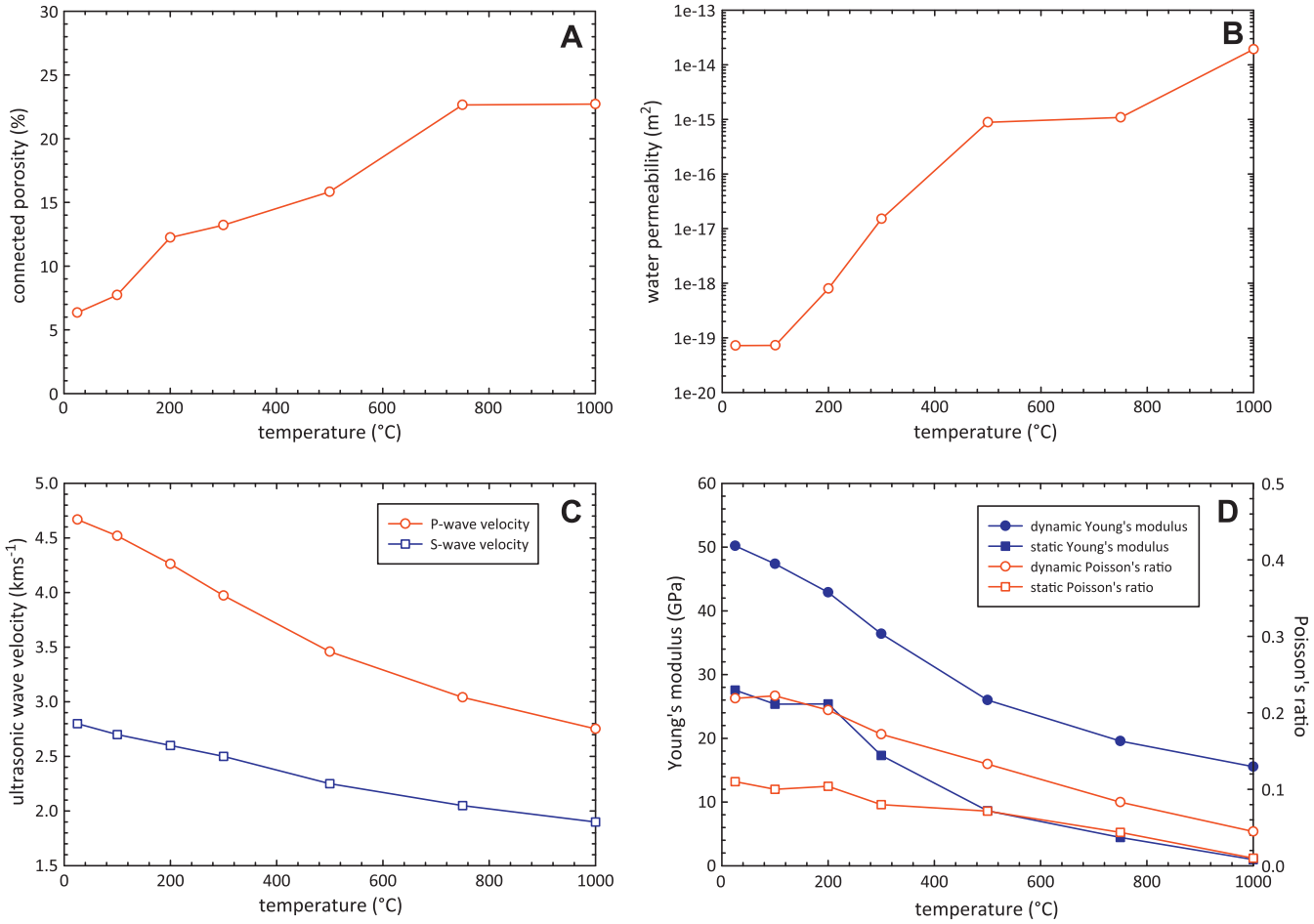

Fig. 14. The influence of thermal-stressing temperature (TST) on the (A) connected porosity, (B) permeability, (C) ultrasonic wave velocities and, (D) static and dynamic elastic moduli in HSC.

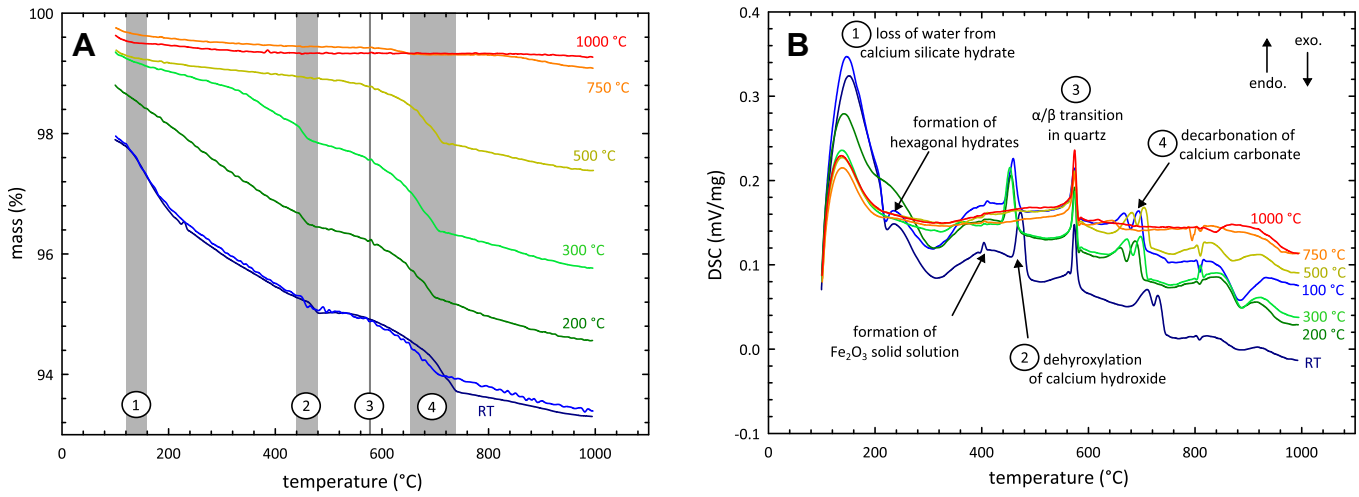

Fig. 15. (A) Thermo-gravimetric (TG) analysis and (B) differential scanning calorimetry (DSC) analysis on powder of the initial HSC (RT), and powders of HSC thermally-stressed to temperatures of 100, 200, 300, 500, 750, and 1000 °C. The main chemical reactions and phase transitions are labelled on both (A) and (B). The grey areas in (A) represent the temperature range for a given reaction.

decarbonation of calcium carbonate (between 650 and 740 °C) do not commence until temperatures much beyond 200 °C (Figs. 15 and 17). Since our TG analysis suggests that the most important reaction, in terms of mass loss, is the dehydration of C–S–H gel, a reaction that reduces sample mass by 3% before 200 °C (the total mass loss over the entire heating range was about 7%), it could be concluded that the residual properties of HSC is influenced more

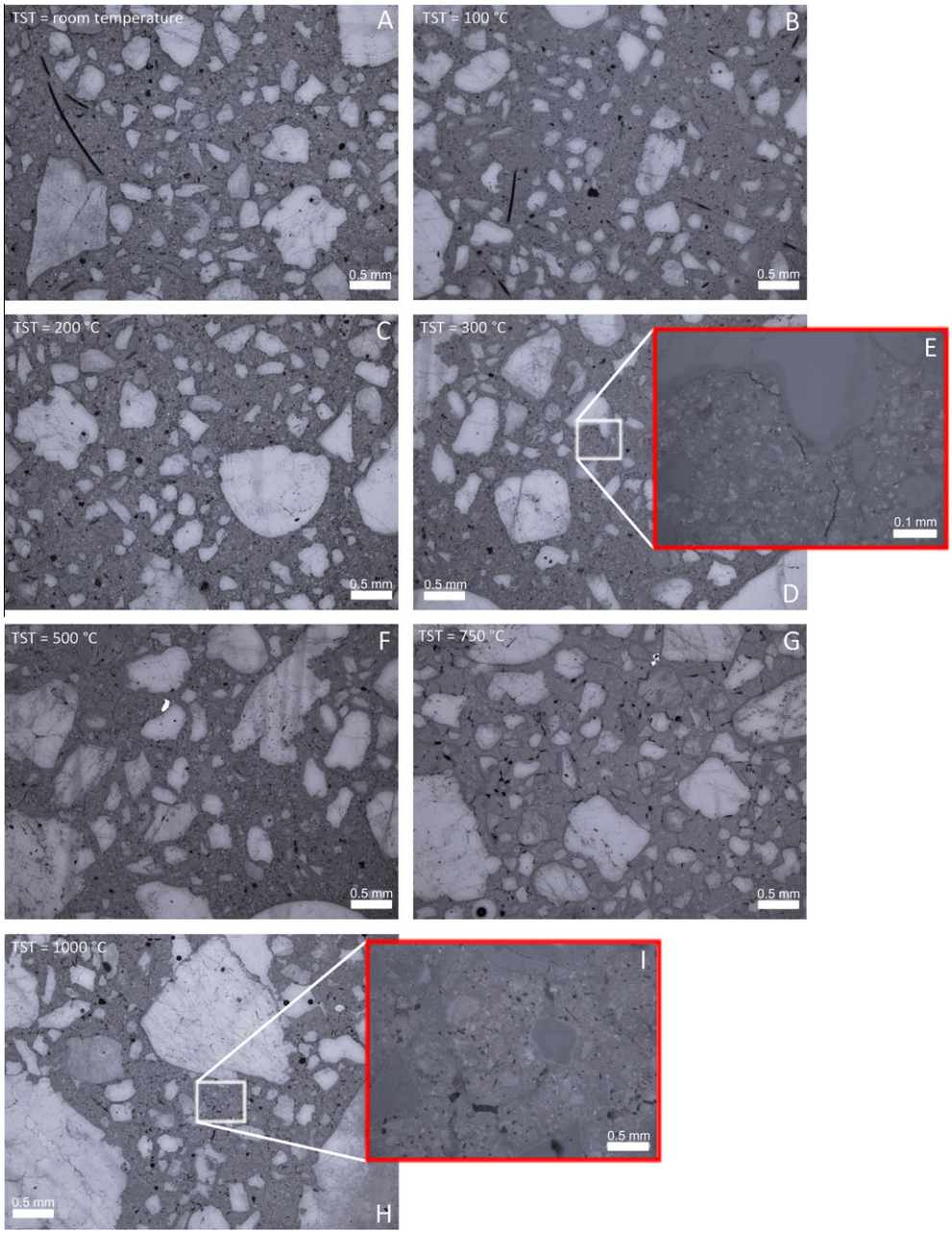

Fig. 16. Photomicrographs, taken in reflected light, of a sample of the initial HSC (A) and samples of HSC thermally-stressed to temperatures of 100 °C (B), 200 °C (C), 300 °C (D), 500 °C (F), 750 °C (G) and, 1000 °C (H). Insets: (E) thermal microcracks present close to silica aggregate particles; (I) the "sponge-like" eroded texture within the cement matrix.

by dehydroxylation of calcium hydroxide and the decarbonation of calcium carbonate than by the dehydration of C–S–H gel. Furthermore, 200 °C is above the melting temperature of the PP fibres, added to reduce the impact of explosive spalling. The void space left by the departed PP fibres could act as "stress concentrators" facilitating the nucleation of microcracks and thus lowering the bulk strength of the sample. A reduction in UCS and tensile strength with increasing temperature (in residual and "hot-test" experiments) has been previously observed for HSC (Fig. 18).

Results from our mechanical tests show that the failure mode changed from macroscopically brittle to increasingly macroscopically ductile (the samples were however, by definition, still brittle, see [67]) for samples subjected to TSTs exceeding 300 °C. Previous studies on HSC in "hot-tests" showed that increased ductility was observed above 600 °C [76]. In our tests, failure was rapid and catastrophic below 300 °C, and accompanied by a dramatic acceleration in AE output and drop in *b*-value. The resulting macrocracks propagated through both the PC matrix and the silicate aggregates (Fig. 13). Above 300 °C, failure was significantly slower and accompanied by a more gradual increase in AE output and an essentially constant *b*-value. Resulting macrocracks were restricted to the PC matrix, and did not fracture the siliceous aggregates (Fig. 13). We also see that the strain at failure increases significantly for TSTs above 300 °C, even though the failure stresses (i.e., strengths) are dramatically lower. This can be explained by the nature of the thermal microcrack population. With each increase in TST, a larger population of thermally-induced microcracks is generated, and these microcracks are

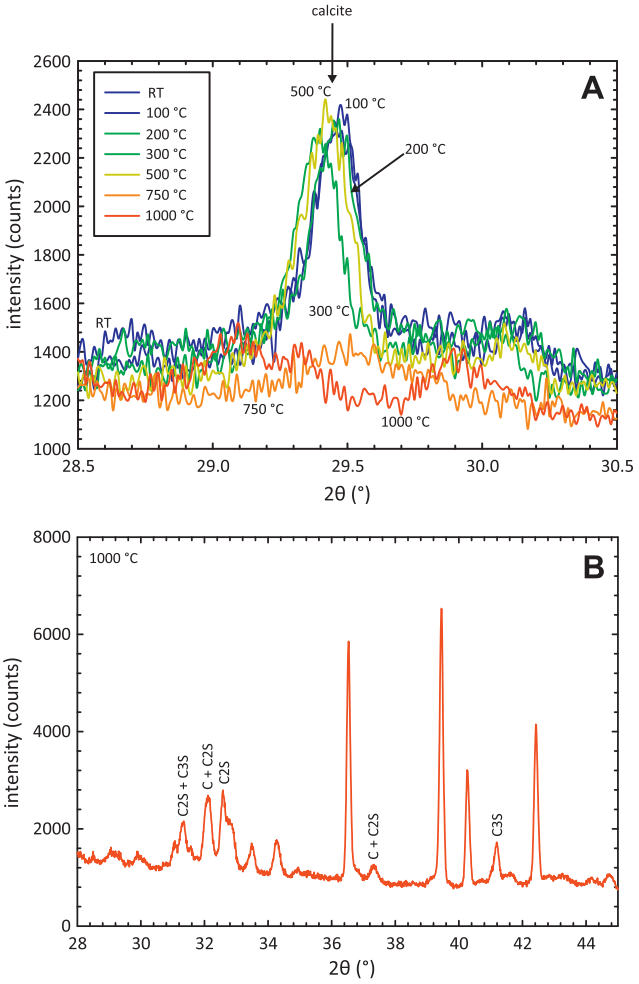

Fig. 17. (A) X-ray diffraction (XRD) spectra between the 2θ angles of 28.5° and 30.5° for a powder of the initial HSC (RT) and powders of HSC thermally-stressed to temperatures of 100, 200, 300, 500, 750, and 1000 °C. (B) XRD spectra between the 2θ angles of 28° and 45° for a powder of PC thermally-stressed to 1000 °C. The labels are abbreviated according to cement chemist notation.

likely to be isotropically distributed (e.g., see [77]). These cracks are still present after the samples are cooled to room temperature, thus making the samples heated to the highest temperatures more compliant than those heated to more modest temperatures. This is confirmed by the reduction in Young's modulus with increasing TST (Fig. 14D). When the samples are subsequently mechanically stressed during the UCS tests, thermal microcracks that are oriented parallel to the axial stressing direction open preferentially. So samples with more thermal microcrack damage (higher TST) accommodate more axial strain and develop more radial strain than samples with less thermal crack damage (lower TST). Since it is the axial microcracks that open preferentially, the radial strain increases more rapidly than the axial strain; hence there is a commensurate increase in volumetric strain. In contrast, we see that the displacement at which the first fracture occurs in our tensile experiments remains essentially constant (between 0.15 and 0.20 mm) regardless of TST. This difference simply reflects the different manner in which compressive and tensile failure occurs. Compressive failure occurs by the propagation, linkage and coalescence of many microcracks to produce a complex fracture damage zone. By contrast, tensile failure is a simpler process involving growth and linkage of the few largest and most favourably oriented cracks. This difference in failure complexity also explains why the compressive strength of brittle materials is some 8–12 times higher the tensile strength (see [71]).

Volumetric strain data from our UCS tests also show the stress at which C′ (the onset of dilatancy, see [70]) occurred decreased with increasing TST (Fig. 9B). However, it has been observed previously that the position of C′ did not change during increasing-amplitude, stress cycling experiments designed to impart incremental microcrack damage on a sample (see [64,78,79]). Again, this can be explained by the nature of the microcrack populations. In the stress-cycling tests, an anisotropic microcrack network develops, sub-parallel to the greatest principal stress. The formed stress-induced microcracks, which close during unloading on the previous cycle, re-open elastically to produce a dilatant volume increase during increased loading on the current cycle. This re-opening occurs at the same level of stress on every cycle irrespective of the level of damage. However, with each thermal-stressing increment, a larger and larger population of thermally-induced isotropic microcracks form. Therefore, the number of microcracks that are favourably orientated to open during uniaxial loading increases with TST. Consequently, as stress is increased upon loading, more thermal microcracks are available to open, resulting in a lower stress for the onset of dilatant behaviour. This interpretation could also explain why we observed a decrease in Poisson's ratio with increasing thermal-stressing (see also [73]), while uniaxial cyclic-stressing experiments have previously reported an increase with increasing damage [64,78,79].

Based on the evidence presented in this paper, we suggest that the change in mode of failure and fracture geometries, and the observed deterioration in physical properties, is largely due to the thermally-induced degradation of the PC matrix rather than thermal microcracking in the siliceous aggregates. Firstly, the macrocracks were restricted to the PC matrix at high TSTs (Fig. 13), and secondly, our microstructural analysis has shown that the siliceous aggregates are somewhat unaffected by thermal-stressing (Fig. 16); an observation also observed in SEM studies of thermal damage in concretes [72]. It is likely that the thermal expansion of quartz during the α/β transition was accommodated by the already-weakened PC matrix, imparting additional damage onto the matrix (thus explaining the lack of an extensive microcrack network in the siliceous aggregates). In dense rock such as granite, where there is no heating-induced chemical weakening, the stresses can build sufficiently to fracture the quartz grains [45]. However, in our HSC, where there is significant PC matrix weakening, the thermal stresses are simply transmitted to the PC matrix and never escalate sufficiently to fracture the quartz grains. The notion that the deterioration of HSC physical and mechanical properties is largely due to the thermally-induced degradation of the PC matrix is supported by Fig. 19. Fig. 19 shows the same data as in Fig. 18B, but, this time, the data are classified by the type of aggregate used to prepare the HSC (siliceous, granite, carbonate, or basalt). It can be seen from Fig. 19 that there is no obvious relationship between the type of aggregate and the reduction in strength. Cheng et al. [76] also found that the strength reduction with temperature was similar in siliceous-aggregate and carbonate-aggregate HSC; although, the carbonate-aggregate obtained larger strains before failure. Further, studies have shown that the performance of HSC at elevated temperatures is enhanced by using pozzolanic cements rather than PC, particularly at temperatures below 600 °C [15]. Although, caution to proceed is required, since pozzolanic cements prepared with certain zeolitic tuffs (namely those that contain chabazite and analcime) could reduce their performance at elevated temperatures (see [80]).

Our data also show that thermal microcracking in HSC is more prevalent during the cooling stage of our thermal-stressing experiment (Fig. 6). Previous studies have largely attributed changes in residual material properties during thermal-stressing on thermal

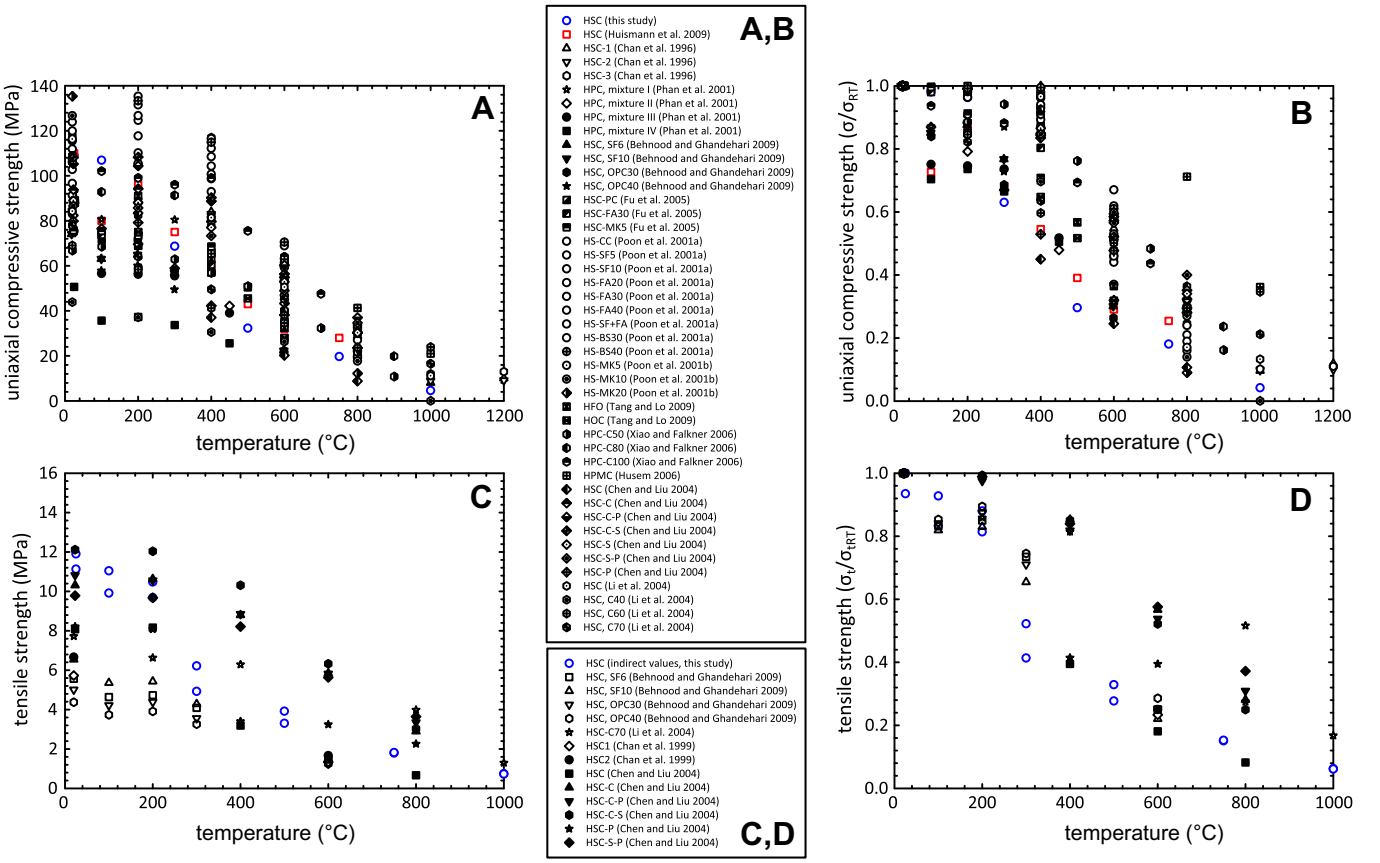

Fig. 18. Compilation of selected data, including those of this study, on (A) the UCS and (C) the tensile strength of various high-strength concretes with increasing temperature, including the data of this study. Normalised plots (with respect to the strength at room temperature) are given in (B) and (D).

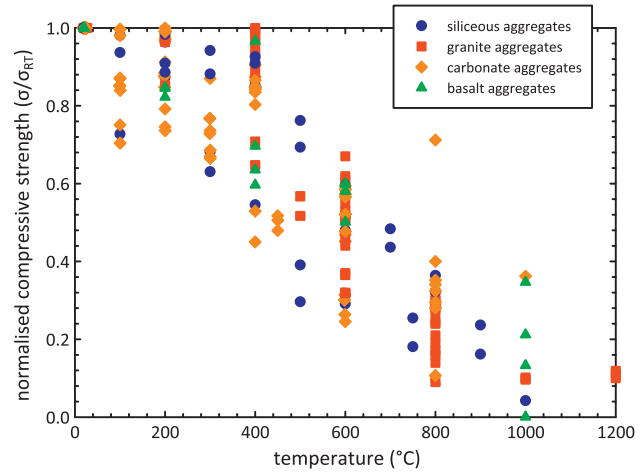

Fig. 19. The same compilation of data as in Fig. 18B, but grouped by the type of aggregate. Filled (blue) circles – siliceous aggregates; filled (red) square – granite aggregates; filled (orange) diamonds – carbonate aggregates; filled (green) triangles – basalt aggregates. (For interpretation of the references to color in this figure legend, the reader is referred to the web version of this article.)

expansion mismatches; however, our study suggests that microcracking caused by the thermal contraction of minerals is as, if not more, important. This observation has been previously observed in porcelain [81], but has not been reported in previous studies on thermal microcracking in materials such as rock or concrete. This can perhaps explain the discrepancy between the residual (this study) and "hot-test" UCS [5] in HSC at temperatures of 300 °C and above (Fig. 12). Since the residual samples have been allowed to cool, and as such contain many more microcracks, they should be weaker than samples deformed at *in situ* temperatures above the temperature required to initiate thermal microcracking (i.e., 180 °C). The "hot-test" data from Huismann et al. [5] on the same HSC show that there is a large decrease in strength at 120 °C, followed by an increase in strength at 200 °C, after which the strength decreases with each temperature increment up to 750 °C (Fig. 12). The large reduction in strength at 100 °C has been previously explained by [82] as due to the reduction of surface energy due to the wetting of the inner concrete surfaces. However, as this moisture is removed at 200 °C, there is a relative increase in surface energy and therefore strength increases from 100 to 200 °C. This is consistent with other studies on HSC during residual tests [13,25]. For studies that measured both residual and "hot-test" UCS, the drop in strength at 100 °C is generally seen to be less in residual experiments than for "hot-test" experiments [17]. However, the residual measurements of this study only show a strength decrease with temperature. This is likely to be due to the fact that the samples used in this study had sufficient chance to dry, due to a combination of (1) leaving the samples for one month prior to testing and, (2) the sample size used in this study were smaller than those used for the above-mentioned studies.

Our results indicate that thermal microcracking (during both heating and cooling) in HSC is dominated by a high proportion of small microcracking events, as evidenced by high *b*-values (between 1.8 and 2, see Fig. 6). Much higher than those reported for HSC immediately prior to macroscopic sample failure in our constant strain rate experiments (as low of 0.7, see Fig. 8). Our study has also illustrated that the Kaiser "temperature-memory" effect holds for HSC (Fig. 7). An observation previously only seen in experiments on rocks and material composites (e.g., [6,47,48,83]).

The fact that the Kaiser "temperature-memory" effect holds for HSC suggests that once a HSC building or structure has experienced a heating event, although the concrete will be considerably weakened, subsequent heating events (assuming they are of a similar temperature) are unlikely to induce further thermal microcrack damage. We propose that this observation is used in the damage characterisation of HSC structures that have experienced multiple heating episodes.

An increase in the connected porosity (Fig. 14A) and permeability (Fig. 14B) of HSC could also have further detrimental repercussions, by increasing the ease at which water can infiltrate. Firstly, the presence of water within material is known to reduce its strength (e.g., [84]) by (1) the reduction of surface free energy as the result of the absorption of pore fluid onto the internal pore surfaces [85] and, (2) subcritical crack growth processes [86]. Stress corrosion (one of the dominant mechanisms of subcritical crack growth) has already been earmarked, albeit theoretically, as an important consideration in the slow deterioration of rock panels in buildings and structures [87] and has even been observed in a high-strength and ultra low permeability concrete used for underground radioactive waste storage [88] and in high performance [89] and regular concrete [90]. We suggest that future studies focus on the time-dependent deformation behaviour of HSC, a phenomenon known as brittle creep [91].

4.3. Implications for buildings and structures made from HSC

Buildings and structures made from, or containing, HSC can be exposed to very high temperatures (in excess of 1000 °C) in the event fire, engulfment by lava flow, and nuclear meltdown. Our study demonstrates that HSC buildings and structures will be jeopardized after a high-temperature event, albeit only if temperatures exceed 200 °C. At 200 °C and below, HSC will retain its competence. Our data also suggests that once a HSC building or structure has experienced a heating event, although the concrete will be considerably weakened, subsequent heating events (assuming they are of a similar temperature) are unlikely to induce further thermal microcrack damage (see discussion above). Our study has highlighted that the thermal liability of the PC matrix is the main reason for the reduction in residual strength and the degradation of HSC physical properties. We suggest that alternative cements should be used to enhance the performance of HSC with increasing temperature; for example, Poon et al. [15] have shown that HSC with pozzolanic cements may perform better than those with PC.

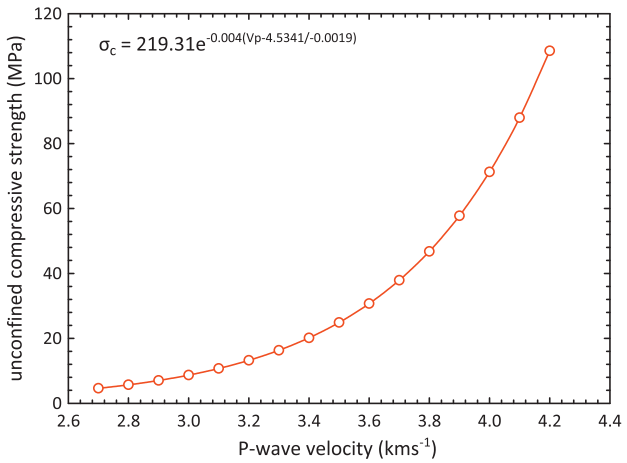

Fig. 20. Monitoring thermal damage in HSC using the relationship between uniaxial compressive strength (UCS) and P-wave velocity.

It has been suggested that the monitoring of *b*-values could be used as a method for tracking progressive damage in concrete bridges [92]. The suggestion is that *b*-values could be used to diagnose the degree and type of degradation in concrete beams; with high *b*-values implying only distributed microcracking, and low *b*-values implying a change to macrocracking and increased risk of failure. However, our results suggest that, where any HSC structure has been subjected to a heating event then the deformation departs from macroscopically brittle behaviour and *b*-values remain high and do not decrease as failure is approached. Under such circumstances, monitoring *b*-values would therefore not be effective.

Ultrasonic waves have long been used to monitor concrete structures [93,94]. They have been used to investigate damage caused by freeze–thaw cycling and salt-scaling [95], chemical damage [96] and damage caused by compressive loads [97,98]. However, since thermal damage is generally considered to be isotropic (e.g., [77]), a function that defines the relationship between strength and ultrasonic wave velocities during compression experiments, as per Qasrawi [98], will not be applicable for thermal damage. Here therefore we suggest a non-destructive means to monitor thermal damage in HSC buildings and structures, using the relationships between the UCS and P-wave velocity, and increasing TST. The relationship between USC and TST was adequately fitted (R^2 value of 0.97) to an exponential function (excluding the data up to 200 °C where only a very modest change in UCS was observed), whilst the relationship between P-wave velocity and TST was fitted to a linear function (R^2 value of 0.97), again excluding data up to 200 °C. Simple substitution yields the relationship:

$$\sigma_c = 219.31e^{-0.004\left(\frac{V_p - 4.5341}{-0.0019}\right)} \quad (5)$$

where σ_c is the UCS and V_p is the measured P-wave velocity. This relationship is plotted in Fig. 20. Therefore, after a thermal damage event, the strength of a HSC structure can easily be assessed by using two piezoelectric transducers, an oscilloscope, and a pulser/receiver. This is a simple, inexpensive, and portable method for monitoring the thermal damage of HSC buildings and structures.

5. Conclusions

1. Thermal microcracking, dominated by small microcracking events, initiates in HSC at about 180 °C and continues until the HSC returns to room temperature. Further, there is more thermal microcracking during cooling, potentially explaining the discrepancy between residual and "hot-test" measurements. HSC also exhibits the Kaiser "temperature-memory" effect (i.e., the previous maximum temperature must be exceeded in order to generate new thermal microcracks).
2. An increase in temperature results in chemical changes/phase transitions within the PC matrix and siliceous aggregates comprising the HSC. The PC matrix undergoes C–S–H gel dehydration between 140 and 160 °C, dehydroxylation of calcium hydroxide between 440 and 480 °C, and decarbonation of calcium carbonate between 650 and 740 °C. All three are commensurate with a loss in sample mass. Confirmation that these reactions progressed was provided by XRD analysis. The siliceous aggregates experience the α/β transition at 573.5 °C which further weakens the PC matrix. Thermally-stressing HSC to 1000 °C results in a total mass loss of about 7%.
3. Thermal-stressing results in a reduction in the strength of HSC. Over the entire range of TSTs (from ambient temperature to 1000 °C), the residual UCS was reduced by 96% and residual ITS

by 94%. However, changes are only very modest until after 200 °C. Changes in the other measured physical properties (connected porosity, permeability, ultrasonic wave velocities, and static and dynamic elastic moduli), in general, also mirror this trend. These results can be explained by (1) AE analysis has shown that 180 °C represents the lower limit for the initiation of thermal microcracking, corroborated by our microstructural observations and, (2) chemical changes to the PC matrix, such as dehydroxylation of calcium hydroxide (between 440 and 480 °C) and decarbonation of calcium carbonate (between 650 and 740 °C), do not commence until temperatures much beyond 200 °C.

4. The mechanical behaviour of the deforming HSC also changes with increasing TST, changing from macroscopically brittle behaviour to increasingly macroscopically ductile behaviour. Below 300 °C, failure is rapid and violent, and accompanied by a dramatic acceleration in AE output and drop in *b*-value. The resulting macrocracks propagate through both the PC matrix and the silicate aggregates. Above 300 °C, failure is significantly slower and accompanied by a more gradual increase in AE output and an essentially constant *b*-value.
5. Based on our data, we suggest that the change in mode of failure and fracture geometries, and the observed deterioration in physical properties, is largely due to the thermally-induced degradation of the PC matrix, rather than thermal microcracking in the siliceous aggregates. Firstly, the macrocracks were restricted to the PC matrix at high TSTs and, secondly, our microstructural analysis has shown that the siliceous aggregates are somewhat unaffected by thermal-stressing. A compilation of previous work, including the data of this study, also suggests that the strength reduction upon heating is unrelated to aggregate-type.
6. Using the relationships between UCS and P-wave velocity and increasing TST we present a non-destructive means to monitor thermal damage in HSC buildings and structures. Upon measuring the P-wave velocity after a heating event, the strength can be deduced using the relationship:

$$\sigma_c = 219.31e^{-0.004}\left(\frac{V_p - 4.5341}{-0.0019}\right)$$

where σ_c is the peak compressive strength and V_p is the measured P-wave velocity.

Acknowledgments

We gratefully acknowledge John Bowles for the design and construction of the radial strain jig, Steve Boon for development and implementation of the load control system, Neil Hughes for help and support during experimentation (all at UCL), and Markus Sieber for his assistance at LMU. M. Heap was funded by the German Federation of Materials Science and Engineering (BV MatWerk) and the German Research Foundation (DFG). D.B. Dingwell acknowledges support of a Research Professorship (LMUexcellent) of the Bundesexzellenzinitiative and the EVOKES advanced grant of the ERC. We would like to thank Rosie Smith for her help with the AE analysis, and Tom Mitchell for organizing the thin section preparation at Ruhr Universität Bochum. We acknowledge the helpful comments of our editor, P.A.M. Basheer, and a host of anonymous reviewers.

References

[1] Bhatty JI. A review of the applications of thermal analysis to cement-admixture systems. Thermochim Acta 1991;189:313–50.
[2] Sha W, O'Neill EA, Guo Z. Differential scanning calorimetry study of ordinary Portland cement. Cem Concr Res 1999;29:1487–9.
[3] Samtani M, Dollomore D, Alexander KS. Comparison of dolomite decomposition kinetics with related carbonates and the effect of procedural variables on its kinetic parameters. Thermochim Acta 2002;392–393:135–45.
[4] Alonso C, Fernandez L. Dehydration and rehydration processes of cement paste exposed to high temperature environments. J Mater Sci 2004;39:3015–24.
[5] Huismann S, Weise F, Schneider U. Influence of preload on the mechanical properties of high strength concrete at high temperatures. In: 1st International workshop 'concrete spalling due to fire exposure', 3–5 September 2009, Leipzig.
[6] Yong C, Wang C-Y. Thermally induced acoustic emission in Westerly granite. Geophys Res Lett 1980;7(12):1089–92.
[7] Kalifa P, Chéné G, Gallé C. High-temperature behaviour of HPC with polypropylene fibres from spalling to microstructure. Cem Concr Res 2001;31:1487–99.
[8] Phan LT, Carino NJ. Review of mechanical properties of HSC at elevated temperature. J Mater Civ Eng 1998:10 [Paper No. 15502].
[9] Chan SYN, Peng G-F, Chan JKW. Comparison between high strength concrete and normal strength concrete subjected to high temperature. Mater Struct 1996;29:616–9.
[10] Chan YN, Peng GF, Anson M. Residual strength and pore structure of high-strength concrete and normal strength concrete after exposure to high temperatures. Cem Concr Res 1999;21:23–7.
[11] Chan SYN, Luo X, Sun W. Compressive strength and pore structure of high-performance concrete after exposure to high temperature up to 800 °C. Cem Concr Res 2000;30:247–51.
[12] Luo X, Sun W, Chan YN. Effect of heating and cooling regimes on residual strength and microstructure of normal strength and high-performance concrete. Cem Concr Res 2000;30:379–83.
[13] Hoff G, Bilodeau A, Malhotra VM. Elevated temperature effects on HSC residual strength. Concr Int 2000;22:41–7.
[14] Phan LT, Lawson JR, Davis FL. Effects of elevated temperature exposure on heating characteristics, spailing, and residual properties of high performance concrete. Mater Struct 2001;34:83–91.
[15] Poon CS, Azhar S, Anson M, Wong YL. Comparison of the strength and durability performance of normal- and high-strength pozzolanic concretes at elevated temperatures. Cem Concr Res 2001;31:1291–300.
[16] Poon CS, Azhar S, Anson M, Wong Y-L. Strength and durability recovery of fire-damaged concrete after post-fire-curing. Cem Concr Res 2001;31:1307–18.
[17] Phan LT, Carino NJ. Effects of test conditions and mixture proportions on behavior of high-strength concrete exposed to high temperatures. ACI Mater 2002;99:54–66.
[18] Li M, Qian C-X, Sun W. Mechanical properties of high-strength concrete after fire. Cem Concr Res 2004;34:1001–5.
[19] Chen B, Liu J. Residual strength of hybrid-fiber-reinforced high-strength concrete after exposure to high temperatures. Cem Concr Res 2004;34:1065–9.
[20] Fu YF, Wong TL, Poon CS, Tang CA. Stress–strain behaviour of high-strength concrete at elevated temperatures. Mag Concr Res 2005;57:535–44.
[21] Husem M. The effects of high temperature on compressive and flexural strengths of ordinary and high-performance concrete. Fire Safety J 2006;41:155–63.
[22] Xiao J, Falkner H. On residual strength of high-performance concrete with and without polypropylene fibres at elevated temperatures. Fire Safety J 2006;41:115–21.
[23] Yan X, Li H, Wong Y-L. Assessment and repair of fire-damaged high-strength concrete: strength and durability. J Mater Civ Eng 2007;19. http://dx.doi.org/10.1061/(ASCE)0899-1561(2007) 19:6(462).
[24] Raju MP, Roa KS, Raju PSN. Compressive strength of heated high-strength concrete. Mag Concr Res 2007;59:79–85.
[25] Behnood A, Ghandehari M. Comparison of compressive and splitting tensile strength of high-strength concrete with and without polypropylene fibers heated to high temperatures. Fire Safety J 2009;44:1015–22.
[26] Noumowé A, Siddique R, Ranc G. Thermo-mechanical characteristics of concrete at elevated temperatures up to 310 °C. Nucl Eng Des 2009;239:470–6.
[27] Tang WC, Lo TY. Mechanical and fracture properties of normal and high-strength concretes with fly ash after exposure to high temperatures. Mag Concr Res 2009;61:323–30.
[28] Siddique R, Noumowé A. An overview of the properties of high-strength concrete subjected to elevated temperatures. Indoor Built Environ 2010;19:612–22.
[29] Khoury GA. Effect of fire on concrete and concrete structures. Progr Struct Eng Mater 2001;2:429–47.
[30] Homand-Etienne F, Troalen J-P. Behaviour of granites and limestones subjected subjected to slow and homogenous temperature changes. Eng Geol 1984;20:219–33.
[31] Chen L-J, He J, Chao J-Q, Qin B-D. Swelling and breaking characteristics of limestone under high temperatures. Min Sci Technol 2009:503–7.
[32] Mao X-B, Zhang L-Y, Li T-Z, Liu H-S. Properties of failure mode and thermal damage for limestone at high temperatures. Min Sci Technol 2009:290–4.
[33] Ohtsu M. The history and development of acoustic emission in concrete engineering. Mag Concr Res 1996;48:321–30.
[34] Ouyang C, Landis E, Shah SP. Damage assessment in concrete using quantitative acoustic emission. J Eng Mech 1991;117:2681–98.

[35] Katsaga T, Sherwood EG, Collins MP, Young RP. Acoustic emission imaging of shear failure in large reinforced concrete structures. Int J Fract 2007;148:29–45.
[36] Li Z, Shah SP. Localisation of microcracking in concrete under uniaxial tension. ACI Mater J 1994;91:372–81.
[37] Maji A, Shah SP. Process zone and acoustic-emission measurements in concrete. Exp Mech 1988;28:27–33.
[38] Ohtsu M, Okamoto T, Yuyama S. Moment tensor analysis of acoustic emission for cracking mechanisms in concrete. ACI Mater J 1998;95:87–95.
[39] Yuyama S, Li Z-W, Ito Y, Arazoe M. Quantitative analysis of fracture process in RC column foundation by moment tensor analysis of acoustic emission. Constr Build Mater 1999;13:87–97.
[40] Kawasaki Y, Tomoda Y, Ohtsu M. AE monitoring of corrosion process in cyclic wet-dry test. Constr Build Mater 2010;24:2353–7.
[41] Grosse C, Reinhardt H, Dahm T. Localization and classification of fracture types in concrete with quantitative acoustic emission measurement techniques. NDT E Int 1997;30:223–30.
[42] Ohtsu M, Uchida M, Okamoto T, Yuyama S. Damage assessment of reinforced concrete beams qualified by acoustic emission. ACI Struct J 2002;99:411–7.
[43] Schokouhi P, Zoëga A, Wiggenhauser H. Nondestructive evaluation of damage in concrete under uniaxial compression. In: Thompson DO, Chimenti DE, editors. Review of quantitative nondestructive evaluation, vol. 29. American Institute of Physics; 2010. p. 1525–32.
[44] Wang HF, Bonner BP, Calrson SR, Kowallis BJ, Heard HC. Thermal stress cracking in granite. J Geophys Res 1989;94(B2):1745–58.
[45] Glover PWJ, Baud P, Darot M, Meredith PG, Boon SA, LeRevelec M, et al. a/b phase transition in quartz monitored using acoustic emissions. Geophys J Int 1995;120:775–82.
[46] Meredith PG, Knight KS, Boon SA, Wood IG. The microscopic origin of thermal cracking in rocks: an investigation by simultaneous time-of-flight neutron diffraction and acoustic emission monitoring. Geophys Res Lett 2001;28(10):2105–8.
[47] Zuberek WM, Zogala B, Dubiel R, Pierwola J. Maximum temperature memory in sandstone and mudstone observed with acoustic emission and ultrasonic measurements. Int J Rock Mech Min Sci Geomech Abstr 1999;35(4/5):416–7.
[48] Choi N-K, Kim T-W, Rhee KY. Kaiser effects in acoustic emission from composites during thermal cyclic-loading. NDT E Int 2005;38:268–74.
[49] David C, Menéndez B, Darot M. Influence of stress-induced and thermal cracking on physical properties and microstructure of La Peyratte granite. Int J Rock Mech Min Sci 1999;36:433–48.
[50] Chaki S, Takarli M, Agbodjan WP. Influence of thermal damage on physical properties of a granite rock: porosity, permeability and ultrasonic wave evolutions. Constr Build Mater 2008;22:1456–61.
[51] Poon CS, Azhar S, Anson M, Wong Y-L. Performance of metakaolin concrete at elevated temperatures. Cem Concr Compos 2003;25:83–9.
[52] Noumowé AN, Siddique R, Debicki G. Permeability of high-performance concrete subjected to elevated temperature (600 °C). Constr Build Mater 2009;23:1855–61.
[53] Gallé C, Sercombe J. Permeability and pore structure evolution of silicocalcareous and hematite high-strength concretes submitted to high temperatures. Mater Struct 2001;34:619–28.
[54] Janotka I, Lubomir B. Pore structures, permeabilities, and compressive strengths of concrete at temperatures up to 800 °C. ACI Mater J 2002;99:196–200.
[55] Hess K-U, Cordonnier B, Lavallée Y, Dingwell DB. High-load, high-temperature deformation apparatus for synthetic and natural silicate melts. Rev Sci Instrum 2007;10(1063/1):2751398.
[56] Gutenberg B, Richter CF. Magnitude and energy of earthquakes. Nature 1955;176:795–6.
[57] Gutenberg B, Richter CF. Magnitude and energy of earthquakes. Ann Geophys (Rome) 1956;9:1–15.
[58] Aki K. Maximum likelihood estimate of b in the formula $\log N = a - bM$ and its confidence limits. Bull Earthq Res Inst 1965;43:237–9.
[59] Main IG, Meredith PG, Jones C. A reinterpretation of the precursory seismic *b*-value anomaly from fracture mechanics. Geophys J Int 1989;96:131–8.
[60] Meredith PG, Main IG, Jones C. Temporal variations in seismicity during quasi-static and dynamic rock failure. Tectonophysics 1990;175:249–68.
[61] Sammonds PR, Meredith PG, Main IG. Role of pore fluids in the generation of seismic precursors to shear fracture. Nature 1992;359:228–30.
[62] Smith R, Sammonds PR, Kilburn CRJ. Fracturing of volcanic systems: experimental insights into pre-eruptive conditions. Earth Planet Sci Lett 2009;280. 221-219.
[63] SM for determining tensile strength of rock materials – 1978 [EUR 4], Part 2 – SM for determining indirect tensile strength by the brazil test. In: Ulusay R, Hudson JA, editors. The complete ISRM suggested methods for rock characterization, testing and monitoring: 1974–2006; 2007 [ISBN 978-975-93675-4-1].
[64] Heap MJ, Faulkner DR. Quantifying the evolution of static elastic properties as crystalline rock approaches failure. Int J Rock Mech Min Sci 2008;45:564–73.
[65] Kolzenburg S, Heap MJ, Lavallée Y, Russell JKR, Meredith PG, Dingwell DB. Strength and permeability recovery of tuffisite-bearing andesite. Solid Earth 2012;3:191–8.
[66] Guéguen Y, Palciauskas V. Introduction to the physics of rocks. Princeton University Press; 1994, ISBN 9780691034522.
[67] Rutter E. On the nomenclature of mode of failure transitions in rocks. Tectonophysics 1986;122:381–7.
[68] Hatton CG, Main IG, Meredith PG. A comparison of seismic and structural measurements of scaling exponents during tensile subcritical crack growth. J Struct Geol 1993;15:1485–95.
[69] Scholz CH. Microfractures, aftershocks, and seismicity. Bull Seismol Soc Am 1968;58:1117–30.
[70] Wong T-F, David C, Zhu W. The transition from brittle faulting to cataclastic flow in porous sandstones: mechanical deformation. J Geophys Res 1997;102:3009–25.
[71] Jaeger J, Cook NGW, Zimmerman R. Fundamentals in rock mechanics. 4th ed. London: Blackwell Publishing; 2007.
[72] Biolzi L, Cattaneo S, Rosati G. Evaluating residual properties of thermally damaged concrete. Cem Concr Compos 2008;30:907–16.
[73] Heap MJ, Mollo S, Vinciguerra S, Lavallée Y, Hess K-U, Dingwell DB, et al. Thermal weakening of the carbonate basement under Mt. Etna volcano (Italy): implications for volcano instability. J Volcanol Geotherm Res 2012;250:42–60.
[74] Mollo S, Heap MJ, Iezzi G, Hess K-U, Scarlato P, Dingwell DB. Volcanic edifice weakening via decarbonation: a self-limiting process? Geophys Res Lett 2012;36:L15307. http://dx.doi.org/10.1029/2012GL052613.
[75] Mollo S, Vinciguerra S, Iezzi G, Iarocci A, Scarlato P, Heap MJ, et al. Volcanic edifice weakening via devolatilization reactions. Geophys J Int 2011;186:1073–7.
[76] Cheng FP, Kodur VR, Wang TC. Stress–strain curves for high strength concrete at elevated temperatures. J Mater Civ Eng 2004;16:84–94.
[77] Menéndez B, David C, Darot M. A study of the crack network in thermally and mechanically cracked granite samples using confocal scanning laser microscopy. Phys Chem Earth 1999;24(7):627–32.
[78] Heap MJ, Faulkner DR, Meredith PG, Vinciguerra S. Elastic moduli evolution and accompanying stress changes with increasing crack damage: implications for stress changes around fault zones and volcanoes during deformation. Geophys J Int 2010;183:225–36.
[79] Heap MJ, Vinciguerra S, Meredith PG. The evolution of elastic moduli with increasing crack damage during cyclic stressing of a basalt from Mt. Etna volcano. Tectonophysics 2009;471:153–60.
[80] Heap MJ, Lavallée Y, Laumann A, Hess K-U, Meredith PG, Dingwell DB. How tough is tuff in the event of fire? Geology 2012;40:311–4.
[81] Kirchhoff G, Pompe W, Bahr H-A. Structure dependence of thermally induced microcracking in porcelain studied by acoustic emission. J Mater Sci 1982;17:2809–16.
[82] Huismann S. Material behaviour of high strength concrete subjected to thermomechanical loading, Deutscher Ausschuss für Stahlbeton, Berlin; 2010 [in German].
[83] Becker D, Cailleau B, Dahm T, Shapiro S, Kaiser D. Stress triggering and stress memory observed from acoustic emission records in a salt mine. Geophys J Int 2010;182:933–48.
[84] Baud P, Zhu W, Wong T-F. Failure mode and weakening effect of water on sandstone. J Geophys Res 2000;105:16371–89.
[85] Rehbinder PA. . Hardness reducers in drilling (translated from Russian), CSIR, Melbourne; 1948.
[86] Atkinson BK. Subcritical crack growth in geological materials. J Geophys Res 1984;89:4077–114.
[87] Chau KT, Shao JF. Subcritical crack growth of edge and center cracks in facade rock panels subject to periodic surface temperature variations. Int J Solids Struct 2006;43:807–27.
[88] Nara Y, Takada M, Mori D, Owada H, Yoneda T, Kaneko K. Subcritical crack growth and long-term strength in rock and cementitious material. Int J Fract 2010. http://dx.doi.org/10.1007/s10704-010-9455-z.
[89] Schneider U, Chen S-W. The chemomechanical effect and the mechanochemical effect on high-performance concrete subjected to stress corrosion. Cem Concr Res 1998;28(4):509–22.
[90] Schneider U, Nagele E, Dumat F. Stress corrosion initiated cracking of concrete. Cem Concr Res 1986;16:535–44.
[91] Heap MJ, Baud P, Meredith PG, Bell AF, Main IG. Time-dependent brittle creep in Darley Dale sandstone. J Geophys Res 2009. http://dx.doi.org/10.1029/2008JB006212.
[92] Colombo IS, Main IG, Forde MC. Assessing damage of reinforced concrete beam using "*b*-value" analysis of acoustic emission signals. J Mater Civ Eng 2003;15(3):280–6.
[93] Jones R, Fąçąoaru I. Recommendations by the ultrasonic for testing concrete pulse method. Mater Struct 1969;2(4):275–84.
[94] Colombo M, Felicetti R. New NDT techniques for the assessment of fire-damaged concrete structures. Fire Safety J 2007;42:461–72.
[95] Selleck SF, Landis EN, Peterson ML, Shah SP, Achenbach JD. Ultrasonic investigation of concrete with distributed damage. ACI Mater 1998;95:27–36.
[96] Naffa SO, Goueygou M, Piwakowski B, Buyle-Bodin F. Detection of chemical damage in concrete using ultrasound. Ultrasonics 2002;40:247–51.
[97] Berthaud Y. Damage measurements in concrete via an ultrasonic technique: Part I experiment. Cem Concr Res 1991;21:73–82.
[98] Qasrawi HY. Concrete strength by combined nondestructive methods: simply and reliably predicted. Cem Concr Res 2000;30:739–46.